JM PAPERS

Darcy–Forchheimer gravity currents in porous media

Sepideh Majdabadi Farahani[1], Luca Chiapponi[2], Sandro Longo[2] and Vittorio Di Federico[1],†

[1]Department of Civil, Chemical, Environmental, and Materials Engineering, Alma Mater Studiorum Università di Bologna, Viale Risorgimento 2, 40136 Bologna, Italy

[2]Department of Engineering and Architecture, Università degli Studi di Parma, Parco Area delle Scienze 181/A, 43124 Parma, Italy

We theoretically and experimentally study gravity currents of a Newtonian fluid advancing in a two-dimensional, infinite and saturated porous domain over a horizontal impermeable bed. The driving force is due to the density difference between the denser flowing fluid and the lighter, immobile ambient fluid. The current is taken to be in the Darcy–Forchheimer regime, where a term quadratic in the seepage velocity accounts for inertial contributions to the resistance. The volume of fluid of the current varies as a function of time as $\sim T^{\gamma}$, where the exponent parameterizes the case of constant volume subject to dam break ($\gamma = 0$), of constant ($\gamma = 1$), waning ($\gamma < 1$) and waxing inflow rate ($\gamma > 1$). The nonlinear governing equations, developed within the lubrication theory, admit self-similar solutions for some combinations of the parameters involved and for two limiting conditions of low and high local Forchheimer number, a dimensionless quantity involving the local slope of the current profile. Another parameter N expresses the relative importance of the nonlinear term in Darcy–Forchheimer's law; values of N in practical applications may vary in a large interval around unity, e.g. $N \in [10^{-5}, 10^{2}]$; in our experiments, $N \in [2.8, 64]$. Sixteen experiments with three different grain sizes of the porous medium and different inflow rates corroborate the theory: the experimental nose speed and current profiles are in good agreement with the theory. Moreover, the asymptotic behaviour of the self-similar solutions is in excellent agreement with the numerical results of the direct integration of the full problem, confirming the validity of a relatively simple one-dimensional model.

Key words: gravity currents, lubrication theory, porous media

† Email address for correspondence: vittorio.difederico@unibo.it

1. Introduction

Gravity currents (GCs) are generated by density differences and appear when a fluid of given density ρ advances into an ambient fluid of different density $\rho \pm \Delta\rho$, and the flow is primarily horizontal (Simpson 1997).

The phenomenon of GCs, ubiquitous in nature and industrial processes, has generated a large body of literature, very difficult to fully review; examples of partial reviews, geared towards specific topics, are Huppert (1998), Griffiths (2000), Moodie (2002), Huppert (2006), Chowdhury & Testik (2014), Riaz & Cinar (2014), Lauriola *et al.* (2018), Ungarish (2018) and Lube *et al.* (2020).

In particular, gravity-driven flows in porous media, well summarized in the book by Woods (Woods 2015), attract interest given the wealth of associated energy and environmental applications, such as CO_2 sequestration (Huppert & Neufeld 2014), reservoir (oil and gas) engineering (De Loubens & Ramakrishnan 2011), underground hydrogen storage (Sheikhi, Sahu & Flynn 2023), geothermal power production (Woods 1999) and the transport of pollutants such as non-aqueous phase liquids (Schneider *et al.* 2015) in the subsurface environment generated by the chemical, mining (drilling fluids, see Li *et al.* 2005) or nuclear industry.

Gravity currents in porous media are viscosity/buoyancy-dominated and typically propagate over (or below) an impermeable bottom (or top) layer, depending whether the intruding current is heavier or lighter than the ambient fluid. Alternatively, the bottom or top limiting layer can be leaky, due to its permeable nature or to one or more draining fracture(s). The ambient fluid is mostly taken to be homogeneous (for the case of ambient stratifications, see Pegler, Huppert & Neufeld (2016)) and often to be immobile, i.e. neglecting return flows (see e.g. Matson & Hogg 2012); this assumption is typically acceptable in the unconfined schematization, with a current depth much less than the thickness of the host layer. The reference frame is usually non-rotating; the base geometry of the flow can be axisymmetric or plane, the former associated with a line of injecting wells, the latter to a single injection well. For these two base flows, simple similarity solutions by Huppert & Woods (1995) and Lyle *et al.* (2005) are available to describe the intermediate-time behaviour of the current. When the geometry becomes more complicated, the influence of boundaries (Zheng & Stone 2022) or topographic controls (Pegler, Huppert & Neufeld 2013) may be incorporated into the conceptual scheme, leading to semianalytical or numerical solutions of the one-dimensional (1-D) transient propagation.

The search for realism in the conceptualization of GCs in porous media has directed researchers also to consider variants to the flow law commonly adopted, i.e. Darcy's law. On one hand, non-Newtonian behaviour of the intruding fluid was considered, and a corresponding extension to Darcy's law adopted, first upon extending the base solution for plane geometry and Newtonian flow first reported in Huppert & Woods (1995) to power-law rheological behaviour (Di Federico, Archetti & Longo 2012), then upon developing solutions for more complex geometries, boundary conditions and types of flow (Longo *et al.* (2021) and references therein). On the other hand, flow in the vicinity of pumping/injecting wells or in coarse porous media is often best described by a nonlinear equation usually known as Darcy–Forchheimer, where an additional term quadratic in the seepage velocity appears in addition to the linear forcing term incorporating permeability. The term was added empirically by Forchheimer (1901), while theoretical derivations of Darcy, and Darcy–Forchheimer equations from first principles, are reported in Neuman (1977) and Whitaker (1996), respectively.

The Darcy–Forchheimer regime is characteristic, in nature, of conglomerate-confined aquifers, composed of conglomerate, coarse sandstone, as happens in the area of the Ordos Basin (Zhang *et al.* 2011, 2018). Further, non-Darcy flow represents a significant challenge to the productivity of hydraulically fractured reservoirs, including those containing shale gas, tight oil and geothermal water formations (Barree & Conway 2004). Darcy–Forchheimer flow is also relevant in the screening and selection of sites for CO_2 sequestration (Mathias *et al.* 2009*a*), and can be also observed in open-graded asphalt pavements; these provide rapid runoff of rainwater, thereby enhancing safety and visibility (Autelitano *et al.* 2022). In all these examples, an injected fluid may displace an ambient fluid and advance into the porous medium (also) by virtue of density differences. It seems therefore both of practical and of general interest to extend the study of the propagation of GCs in porous media to the Darcy–Forchheimer regime. Here we focus on a sharp interface schematization of the GC, and derive a semianalytical model considering the influence of Forchheimer effects on the propagation of plane GCs in an infinite domain. To the best of our knowledge, the only works on GCs incorporating Darcy–Forchheimer flow are Mathias *et al.* (2009*b*) and the aforementioned study by Mathias *et al.* (2009*a*), simulating CO_2 injection and heat transport in a porous domain of infinite cylindrical geometry and finite height, and taking into account the fluid compressibility; the scheme was modified by Mathias *et al.* (2011) and Mathias, McElwaine & Gluyas (2014) to account for a finite rather than infinite domain. In all these cases, the flow law is used in a purely numerical context, so none of these studies undermines the novelty of the present manuscript. In fact, three important differences are considered here: (i) the geometry is plane rather than radial, as in the former case the high seepage velocities necessary to invoke the Forchheimer correction are more likely to be reached in the whole flow domain than in the latter case; (ii) the aquifer subject to injection is of infinite height, hence the flow is free-surface throughout the entire flow domain, as in the two earliest seminal studies on porous GC (Huppert & Woods 1995; Lyle *et al.* 2005) – this restricts the solution's applicability but renders more plausible the no-flow assumption within the ambient fluid; (iii) no compressibility effects are considered (partially a consequence of the previous assumption), and the emphasis is on the difference with the classical approach using Darcy's law in the first study on porous GCs in plane geometry (Huppert & Woods 1995).

The adoption of the Darcy–Forchheimer expression *in lieu* of Darcy's entails the presence of a second source of nonlinearity in the approach, other than that associated with free-surface flow. The nonlinear flow law is then approximated in two limit cases, corresponding to a local Forchheimer number much lower or larger than unity, respectively; in the former case, the flow law is also linearized. Both cases allow the reduction of the partial differential equation (PDE) governing the 1-D transient flow of the GC to an ordinary differential equation (ODE) and are thus amenable to classical, late-time similarity solutions when coupled with the integral boundary condition describing the increase of the volume of the current as a power of time of exponent γ. Results stemming from the solution of these ODEs compare favourably with those deriving from the numerical integration of the original PDEs.

The paper is organized as follows. In § 2, the fundamentals of Darcy–Forchheimer flow are revised, and the GC problem is formulated in plane geometry. In § 3, the problem is solved in semianalytical form with said approximations for $\gamma \neq 2$, while § 4 presents fully analytical results for $\gamma = 2$. The approximate solutions are corroborated with full numerical results in § 5. Section 6 describes the experiments conducted to check our theoretical models. We draw conclusions and provide indications for future work in § 7. Appendix A provides details on the structure and typical ranges of the dimensionless

parameter summarizing problem parameters and governing the formulation, Appendix B presents an alternative expression for the average slope of the current, while Appendix C illustrates the derivation of the self-similar solution for low local Forchheimer number in a more general context.

2. Materials and methods

2.1. *Darcy–Forchheimer flow in porous media*

High-velocity filtration flow, termed also inertial in the literature (and having nothing to do with inertial GCs), in isotropic porous media is usually described by the Darcy–Forchheimer equation, reading in vectorial form (Forchheimer 1901)

$$\nabla p - \rho \boldsymbol{g} = - \left(\frac{\mu}{k} + \rho \beta \left| \boldsymbol{u} \right| \right) \boldsymbol{u} = - \left(\alpha + \rho \beta \left| \boldsymbol{u} \right| \right) \boldsymbol{u}, \tag{2.1}$$

where p is the pressure, $\boldsymbol{g} \equiv (0, 0, -g)$ is the gravity, $\boldsymbol{u}$ is the Darcy velocity of modulus $|\boldsymbol{u}| = \sqrt{\boldsymbol{u} \cdot \boldsymbol{u}}$, ρ and μ are the fluid density and dynamic viscosity, k ($[k] = [L^2]$) is the medium permeability, $\alpha = \mu/k$ and β ($[\beta] = [L^{-1}]$) is the Forchheimer or inertial factor, having an empirical nature. Literature methods for determining β are either based on direct experimental measurement, or assume a direct correlation between β and other intrinsic properties of the porous medium, such as porosity and permeability (Lenci, Zeighami & Di Federico 2022). On the basis of dimensional analysis, it can be proven that (Autelitano *et al.* 2022)

$$\beta = C_D \left(\frac{\rho g}{\mu K} \right)^{1/2} \equiv \frac{C_D}{k^{1/2}}, \tag{2.2}$$

being $K = (\rho g k)/\mu = g k/\nu$ ($[K] = [L T^{-1}]$) the hydraulic conductivity, $\nu = \mu/\rho$ the kinematic viscosity and C_D the form-drag dimensionless coefficient. More general forms of (2.1) describe flow in anisotropic media (Whitaker 1996; Garibotti & Pészynska 2009); see also Lasseux & Valdés-Parada (2017) for a review of historical developments aimed at representing nonlinear effects in porous media flow.

Equation (2.1) can be formulated in terms of hydraulic head $h = z + p/(\rho g)$ as

$$\nabla h = - \left(\frac{1}{K} + \frac{\beta}{g} \left| \boldsymbol{u} \right| \right) \boldsymbol{u}. \tag{2.3}$$

When $\beta = 0$, (2.1) and (2.3) revert to Darcy's law, governing the purely viscous regime in porous media flow. In practice, the transition between the viscous and the inertial regime is governed by the Forchheimer number $Fo = (k \beta \rho |\boldsymbol{u}|)/\mu$, equal to the ratio of liquid–solid interaction to viscous resistance (Ruth & Ma 1992); values of Fo of order 0.11 entail an error of ignoring non-Darcy behaviour of 10 % according to Zheng & Grigg (2006). Note that k in (2.2) is the Forchheimer permeability k_F, which is close, but not the same as, the Darcy permeability k_D appearing in the isotropic form of Darcy's law $\nabla p - \rho \boldsymbol{g} = -(\mu/k_D) \boldsymbol{u}$ (Muljadi *et al.* 2017; El-Zehairi *et al.* 2019). Henceforth and in the previous relationships, this difference is neglected on grounds of the smallness of the difference $k_F - k_D$ and assume $k_D = k_F = k$ is assumed. Analogously, we neglect a possible influence of the weak inertia regime, which would imply a cubic term in (2.1) *in lieu* of the quadratic one; we do so on the basis of the narrowness of the transition zone between the viscous and inertial regime governed by (2.1) (Fourar *et al.* 2004). The Darcy velocity is derived as a function of the pressure gradient upon inverting (2.1). First, (2.1)

is rewritten as (Auriault, Geindreau & Orgéas 2007)

$$-\boldsymbol{G} = -\boldsymbol{\nabla}(p + \rho g z) \equiv (\alpha + \rho\beta\,|\boldsymbol{u}|)\,\boldsymbol{u}. \tag{2.4}$$

Taking the absolute value of (2.4) yields a second-order algebraic equation in $|\boldsymbol{u}|$, with a single positive root (the negative root is non-physical as the absolute value cannot be negative, note the typo in equation (8) of Auriault *et al.* (2007)); this expression of $|\boldsymbol{u}|$ is back substituted in (2.4) and the expression for $\boldsymbol{u}$ is then derived, yielding

$$\boldsymbol{u} = -\frac{2\boldsymbol{G}}{\alpha\left(\sqrt{1 + \dfrac{4\rho\beta|\boldsymbol{G}|}{\alpha^2}} + 1\right)}. \tag{2.5}$$

Equation (2.5) is pseudolinear in the gradient $\boldsymbol{G}$ of the generalized pressure $p + \rho g z$, but with a constant of proportionality inversely dependent upon the square root of $|\boldsymbol{G}|$: hence, as $|\boldsymbol{G}|$ increases, $|\boldsymbol{u}|$ increases in a less than linear fashion; also, an apparent Forchheimer permeability $k_{AF} = k_{AF}(|\boldsymbol{G}|)$ can be defined to give back the pseudo-Darcy formulation $\boldsymbol{u} = -(k_{AF}/\mu)\boldsymbol{G}$.

The 1-D version of (2.5), written along the horizontal x axis, reads

$$u = -\frac{2G}{\alpha\left(\sqrt{1 - \dfrac{4\rho\beta G}{\alpha^2}} + 1\right)} \equiv \frac{\alpha}{2\rho\beta}\left(\sqrt{1 - \frac{4\rho\beta G}{\alpha^2}} - 1\right), \quad G = \frac{\partial p}{\partial x}. \tag{2.6}$$

The limit of (2.6) for $\beta \to 0^+$ leads back to Darcy's law by virtue of l'Hôpital's rule.

2.2. *Formulation of the problem*

We consider a GC of a fluid advancing on a horizontal, rigid, impermeable plane in a saturated porous domain, as shown in figure 1. The motion is driven by the density difference $\Delta\rho$ between the lighter fluid saturating the porous medium and the heavier intruding fluid. The volume per unit width of the intruding fluid is usually expressed as qt^γ, where q and γ are constant; $\gamma = 0$ and $\gamma = 1$ correspond to a constant volume and a constant flow rate, respectively, and $0 < \gamma < 1$, $\gamma > 1$ represent a waning/waxing inflow rate. Throughout our derivations, we postulate the existence of a representative elementary volume within the porous medium, on the basis of the fact that the average thickness of the current is decidedly larger than the grain size, an assumption that may become critical near the nose of the current, especially for coarse media requiring the adoption of the Darcy–Forchheimer law.

Conventionally, in the study of GCs, capillary forces and surface tension are neglected. Thus, it is assumed that there is no viscous fingering effect and a sharp interface between the two fluids is formed. At high velocity, the mixing between the GC fluid and the ambient fluid can be significant, and at late times this could render the assumption of a sharp interface invalid. Also, lubrication theory is used as a fundamental assumption, stating that the length of the current in one direction is much greater than its extension in other directions.

With these approximations, the current may be described by the horizontal velocity component only, i.e. $\boldsymbol{u} \equiv (u, 0, 0)$, and by its height $h(x, t)$, while the vertical velocity is negligible. It is usually assumed that the ambient fluid is at rest. Pressure within the current may be approximated by a hydrostatic distribution, expressed for $z \le h_0$ as $p(x, z, t) =$
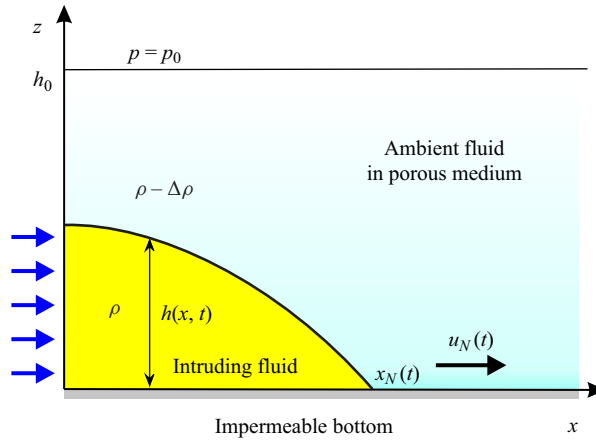
S. Majdabadi Farahani, L. Chiapponi, S. Longo and V. Di Federico

Figure 1. Sketch of a two-dimensional GC intruding into a saturated porous medium.

$p_0 - \Delta\rho\, g(h_0 - h(x, t)) + \rho\, g(h_0 - z)$, where $p_0 = p(z = h_0)$ is a constant and $h(x, t)$ ($\ll h_0$) is the thickness of the ambient fluid. Hence, the pressure and the current height are related via

$$\frac{\partial p}{\partial x} = \Delta\rho\, g\frac{\partial h}{\partial x}, \tag{2.7}$$

and substituting (2.7) into (2.6) gives for the horizontal velocity u

$$u = \frac{\alpha}{2\rho\beta} \left(\sqrt{1 - \frac{4\rho\Delta\rho g\beta}{\alpha^2}\frac{\partial h}{\partial x}} - 1 \right). \tag{2.8}$$

For such 1-D transient flow under the additional assumption of homogeneous porosity, the local mass balance equation linking the velocity to the height of the current reads

$$\frac{\partial(uh)}{\partial x} = -\phi\frac{\partial h}{\partial t}, \tag{2.9}$$

and the governing equations are completed by the global mass balance per unit width and the boundary condition at the current nose, i.e.

$$\phi \int_0^{x_N(t)} h\, \mathrm{d}x = qt^\gamma, \quad h(x_N(t), t) = 0, \tag{2.10a,b}$$

where $x_N(t)$ is the position of the current nose; ϕ is the porosity, q a factor of dimensions $[q] = [L^2 T^{-\gamma}]$ and γ a non-negative real number. The dimensionless form of the variables is $T = t/t_0$, $X = x/x_0$, $X_N = x_N/x_0$, $H = h/x_0$, $U = u/u_0$, where the velocity, time and space scales u_0, t_0, x_0 are

$$u_0 = \frac{\alpha}{\rho\beta\phi}, \quad t_0 = \left(\frac{q}{\phi u_0^2}\right)^{1/(2-\gamma)}, \quad x_0 = u_0 t_0, \tag{2.11a-c}$$

for $\gamma \neq 2$ and $\beta \neq 0$. Other choices of scales are possible, see for example Ciriello et al. (2013); the velocity scale u_0 arises naturally as being proportional to the ratio between the Darcy and the inertial effect in terms of generalized pressure gradient, this can be seen by writing $u_0 = (u_*/\phi)[(\mu u_*)/k]/(\rho\beta u_*^2)$, with u_* a generic reference velocity.

1000 A89-6

The velocity (2.8) becomes in dimensionless form

$$U = \frac{\phi}{2} \left(\sqrt{1 - 4N\frac{\partial H}{\partial X}} - 1 \right), \tag{2.12}$$

and substituting (2.12) into the dimensionless version of (2.9) gives

$$\frac{\partial H}{\partial T} = -\frac{1}{2} \frac{\partial}{\partial X} \left[H \left(\sqrt{1 - 4N\frac{\partial H}{\partial X}} - 1 \right) \right], \tag{2.13}$$

with (2.10a,b) becoming

$$\int_0^{X_N} H \, dX = T^\gamma, \quad H(X_N(T), T) = 0. \tag{2.14a,b}$$

The dimensionless parameter

$$N = \frac{\rho \Delta\rho g \beta}{\alpha^2} \equiv \frac{\rho \Delta\rho g \beta k^2}{\mu^2} \equiv \frac{\Delta\rho}{\rho} \frac{g\beta k^2}{\nu^2} \tag{2.15}$$

expresses the relative importance of the nonlinear term within the PDE (2.13) and recovers the Darcy flow if it tends to zero as a consequence of $\beta \to 0^+$. Here N is a combination of canonical pure numbers in fluid mechanics, as detailed in Appendix A. A similar dimensionless quantity appears in equations (12) and (13) of Auriault *et al.* (2007) except for the relative density difference $\Delta\rho/\rho$; there, $g\beta k^2/\nu^2$ is taken to be of order unity to discuss the upscaling of the Darcy–Forchheimer law. A similar quantity is also defined in Vilarrasa *et al.* (2010) and termed 'gravity number'. The realistic range of variation of N is discussed in Appendix A and spans several orders of magnitude, roughly in the range $N \in [10^{-5}, 10^2]$.

3. Solution for $\gamma \neq 2$

The system of dimensionless governing equations (2.13)–(2.14a,b) valid for $\gamma \neq 2$ is in general amenable to a full numerical solution for a given initial condition, see Zeighami, Lenci & Di Federico (2022) for details. Such a solution is pursued in § 5, while the present Section is devoted to deriving approximate solutions in semianalytical form.

We first seek an approximate similarity solution valid as an intermediate asymptotic (Barenblatt 1952) based on an approximation of the seepage velocity in (2.12) when the dimensionless parameter

$$\zeta = 4N \left| \frac{\partial H}{\partial X} \right| \tag{3.1}$$

becomes both small and large with respect to unity, following Moutsopoulos & Tsihrintzis (2005). Note that ζ has the physical meaning of a local Forchheimer number (Lenci *et al.* 2022) and its magnitude depends on both the N value, which is fixed for a given problem, and the local slope of the GC profile, which varies depending on the location. In particular, for $\zeta \ll 1$, where ζ is small, but not so small that inertial effects on the flow can be disregarded, the quantity $\sqrt{1 + \zeta}$ is approximated by its second-order Taylor's expansion $\sqrt{1 + \zeta} \approx 1 + \zeta/2 - \zeta^2/8$. When, on the other hand, $\zeta \gg 1$, we can either: (i) assume at leading order $\sqrt{1 + \zeta} - 1 \approx \sqrt{\zeta}$ and hence $U \propto \sqrt{|\partial H/\partial X|}$ (Fourar *et al.* 2005; Auriault *et al.* 2007), i.e. the Forchheimer term in (2.6) and (2.12) is dominant with respect to

the Darcy one; or (ii) use a higher-order approximation – the latter option is not pursued here. The correctness of the results deriving from the assumptions on the ζ values can be verified by comparing the approximate results with a full numerical simulation of the problem expressed by (2.13)–(2.14a,b).

3.1. *Low local Forchheimer number ($\zeta \ll 1$)*

Substituting $\sqrt{1+\zeta} \approx 1 + \zeta/2 - \zeta^2/8$ in (2.12) and (2.13) yields at first order

$$U = -\phi N \frac{\partial H}{\partial X}, \tag{3.2}$$

$$\frac{\partial H}{\partial T} = N \frac{\partial}{\partial X}\left(H\frac{\partial H}{\partial X}\right) \tag{3.3}$$

and the mass balance (3.3) takes the classical monomial form of the dimensionless porous medium equation (Vázquez 2007) albeit with the right-hand side modified by the factor N. The mathematical problem given by (3.3) together with (2.14a,b) is amenable to a self-similar solution according to the methodology outlined in Di Federico *et al.* (2012), where their exponent n is equal to unity and their exponent α is our exponent γ. See also the theoretical general procedure detailed in Appendix C.

In order to find similarity solutions, we note that (2.14a,b) and (3.3) provide scaling relationships

$$HX \sim T^\gamma, \quad H \sim X^2 T^{-1}. \tag{3.4a,b}$$

Eliminating H or X from (3.4a,b), the scalings for the current length and height result in

$$X \sim T^{(\gamma+1)/3}, \quad H \sim T^{(2\gamma-1)/3}. \tag{3.5a,b}$$

We therefore introduce the similarity variable and the similarity scaling for the current profile as

$$\xi = XT^{-(\gamma+1)/3}, \quad H(X,T) = N^{-1}\xi_N^2 T^{(2\gamma-1)/3}\Phi(\chi), \tag{3.6a,b}$$

where ξ_N is the unknown value of ξ at the current nose, $\Phi(\chi)$ is the shape function or thickness profile, $\chi = \xi/\xi_N$ is a rescaled similarity variable. From (3.6a,b) the dimensionless length of the current and the speed of propagation of the nose (u_N being its dimensional counterpart) are given by

$$X_N(T) = \xi_N T^{(\gamma+1)/3}, \quad U_N = \frac{\gamma+1}{3}\xi_N T^{(\gamma-2)/3}, \tag{3.7a,b}$$

i.e. the current decelerates if $\gamma < \gamma_c = 2$ and accelerates if $\gamma > \gamma_c = 2$, with γ_c being the critical threshold value of the time exponent γ. Substituting (3.6a,b) in (3.3) and (2.14a,b) yields, respectively,

$$\left(\Phi\Phi'\right)' + \frac{\gamma+1}{3}\chi\Phi' - \frac{2\gamma-1}{3}\Phi = 0, \tag{3.8}$$

$$\xi_N = \left(\frac{1}{N}\int_0^1 \Phi\,\mathrm{d}\chi\right)^{-1/3}, \quad \Phi(1) = 0, \tag{3.9}$$

where the prime indicates the ordinary derivative with respect to χ. Note that for $N = 1$ the analytical model ((3.8)–(3.9)) for a Forchheimer GC seems identical to the one derived for
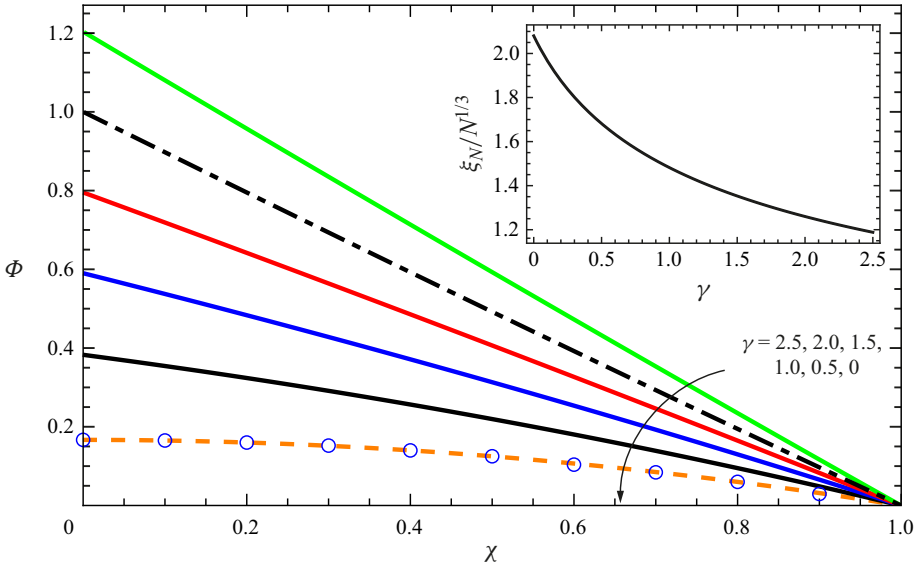
Figure 2. Self-similar solution for low local Forchheimer number, first-order approximation. Shape function Φ as a function of scaled similarity variable χ. Curves represent numerical solutions of (3.8)–(3.9) for γ ranging between 0 and 2.5; open circles represent the analytical solution (3.10) for $\gamma = 0$, the dash dotted straight line is the solution for $\gamma = 2$. The inset shows the value of the prefactor $\xi_N/N^{1/3}$, where $N = 1$ corresponds to the solution by Huppert & Woods (1995).

a Darcy one by Huppert & Woods (1995), see also Ciriello *et al.* (2013) when their $\omega = 1$, but this is a coincidence as the velocity and spatial scales are different, and so are the respective dimensionless forms.

Equation (3.8) with constraints (3.9) can be exactly integrated for the case $\gamma = 0$,

$$\Phi(\chi) = \frac{1}{6}\left(1 - \chi^2\right), \quad \xi_N = (9N)^{1/3}, \tag{3.10}$$

again reducing to the result by Huppert & Woods (1995) and Pattle (1959) for $N = 1$.

For $\gamma \neq 0$, numerical methods must be employed to solve (3.8)–(3.9). A second boundary condition near the nose of the current is introduced for this purpose by expanding (3.8) in Taylor series about $\chi = 1$, finding to first order

$$\Phi = \frac{\gamma + 1}{3}(1 - \chi), \tag{3.11}$$

and

$$\Phi'(1) = -\frac{\gamma + 1}{3}. \tag{3.12}$$

More terms could be added to the expansion, but a numerical solution for $\Phi(\chi)$ is more convenient.

Figure 2 shows the shape function and the prefactor for different values of γ and for $N = 1, 2, 5$, computed in Mathematica 13.2. While the function near the origin increases with γ, the prefactor decreases with γ and N, with an overall combination that collapses to the analytical solution available for $\gamma = 0$.

For the general case $\gamma \neq 0$, the aspect ratio of the current (the ratio between its average thickness $\bar{H}$ and extent X_N) and its average slope are, respectively (see Lauriola *et al.* 2018)

$$S \equiv \frac{\bar{H}}{X_N} = \frac{1}{N}\xi_N T^{(\gamma-2)/3}\bar{\Phi}, \quad \overline{\left|\frac{\partial H}{\partial X}\right|} = \frac{1}{N}\xi_N T^{(\gamma-2)/3}\overline{\left(\frac{d\Phi}{d\chi}\right)}, \quad (3.13a,b)$$

where the overline indicates the average value. Both said quantities are functions of the dimensionless parameter N also via the prefactor ξ_N. In order to dispense with the average value of $\overline{(d\Phi/d\chi)}$, a different (crude) approximation for the average slope is reported in Appendix B.

Appendix C details the approach for deriving higher-order approximations of the similarity solution.

3.1.1. *The solution for $\gamma \to 2$ in the low-Forchheimer-number limit ($\zeta \ll 1$)*

An immediate result from (3.8) is that $\Phi = (1 - \chi)$ with constant $\Phi' = -1$. The slope S and the speed U_N become

$$S = (\xi_N/N)T^{(\gamma-2)/3}, \quad U_N = \xi_N T^{(\gamma-2)/3}, \quad \xi_N = (2N)^{1/3}, \quad (3.14a\text{--}c)$$

with S and U_N that are time independent when $\gamma \to 2$.

These results appear unphysical if we simply set $T^{\gamma-2} = 1$, since S and U_N are constant, as expected, but do not depend on q, whereas we expect that a larger q generates a faster current with higher slope. However, expressing the limit for $T^{\gamma-2}$ for $\gamma \to 2$ in terms of dimensional variables, yields

$$\lim_{\gamma \to 2} T^{\gamma-2} = \lim_{\gamma \to 2} t^{\gamma-2}t_0^{\gamma-2} = \frac{q}{\phi u_0^2} \equiv \delta^{-2}, \quad (3.15)$$

where $\delta = u_0/(q/\phi)^{1/2}$. Hence, (3.14a–c) for $\gamma \to 2$ become

$$S = (\xi_N/N)\delta^{-2/3}, \quad U_N = \xi_N\delta^{-2/3}, \quad \xi_N = (2N)^{1/3}, \quad \text{for } \zeta \ll 1. \quad (3.16)$$

With this new formulation, larger values of q mean lower values of δ, and a faster current of higher slope for increasing q results.

3.2. *High local Forchheimer number ($\zeta \gg 1$ or $\zeta' \ll 1$)*

We rewrite the velocity expression (2.12) as

$$U = \frac{\phi}{2}\sqrt{\zeta}\left(\sqrt{1+\zeta'} - \sqrt{\zeta'}\right), \quad \zeta' = \frac{1}{\zeta}, \quad (3.17)$$

and substituting $\sqrt{1 + \zeta'} \approx 1 + \zeta'/2 - \zeta'^2/8$ in (3.17) we obtain

$$U = \frac{\phi}{2}\sqrt{\zeta}\left(1 - \sqrt{\zeta'} + \frac{\zeta'}{2} - \frac{\zeta'^2}{8}\right), \quad (3.18)$$

which includes the zeroth-, half-, first- and second-order approximations. Substituting (3.18) into the dimensionless version of (2.9) produces the approximate counterpart to

1000 A89-10

(2.13). At zero order, the velocity and the mass balance equations are given by

$$U = \sqrt{N}\phi\sqrt{-\frac{\partial H}{\partial X}}, \tag{3.19}$$

$$\frac{\partial H}{\partial T} = -\sqrt{N}\frac{\partial}{\partial X}\left[H\sqrt{-\frac{\partial H}{\partial X}}\right]. \tag{3.20}$$

The mathematical problem given by (3.20) together with (2.14a,b) is amenable to a self-similar solution according to the methodology outlined in Di Federico *et al.* (2012), where their exponent n is equal to 2 and their exponent α is our exponent γ.

In order to find similarity solutions, we note that (2.14a,b) and (3.20) provide scaling relationships

$$HX \sim T^{\gamma}, \quad H \sim X^3 T^{-2}. \tag{3.21a,b}$$

Eliminating H or X from (3.21a,b), the scaling for the current length and height results in

$$X \sim T^{(\gamma+1)/3}, \quad H \sim T^{(2\gamma-1)/3}. \tag{3.22a,b}$$

We therefore introduce the similarity variable and the similarity scaling for the current profile as

$$\xi = XT^{-(\gamma+2)/4}, \quad H(X,T) = N^{-1}\xi_N^3 T^{(3\gamma-2)/4}\Phi(\chi), \tag{3.23a,b}$$

where ξ_N is the unknown value of ξ at the current nose, $\Phi(\chi)$ is the shape function or thickness profile, $\chi = \xi/\xi_N$ is a rescaled similarity variable. From (3.23a,b) the length of the current and the speed of propagation of the nose are given by

$$X_N(T) = \xi_N T^{(\gamma+2)/4}, \quad U_N = \frac{\gamma+2}{4}\xi_N T^{(\gamma-2)/4}, \tag{3.24a,b}$$

i.e. the current decelerates if $\gamma < \gamma_c = 2$ and accelerates if $\gamma > \gamma_c = 2$. Substituting (3.23a,b) in (3.20) and (2.14a,b) yields, respectively,

$$\left(\Phi\left(-\Phi'\right)^{1/2}\right)' - \frac{\gamma+2}{4}\chi\Phi' + \frac{3\gamma-2}{4}\Phi = 0, \tag{3.25}$$

$$\xi_N = \left(\frac{1}{N}\int_0^1 \Phi\,d\chi\right)^{-1/4}, \quad \Phi(1) = 0, \tag{3.26}$$

where the prime indicates the ordinary derivative with respect to χ.

This analytical model for a Forchheimer GC seems identical, for $N = 1$, to that derived for a shear-thickening GC with rheological index $n = 2$ by Di Federico *et al.* (2012), but again this has no physical implications as the velocity and spatial scales adopted for non-dimensionalization in the two cases are different.

Equation (3.25) with constraints (3.26) can be exactly integrated for the case $\gamma = 0$, obtaining

$$\Phi(\chi) = \frac{1}{12}\left(1 - \chi^3\right), \quad \xi_N = 2N^{1/4}. \tag{3.27}$$

For $\gamma \neq 0$, numerical methods must be employed to solve (3.25)–(3.26). A second boundary condition near the nose of the current is introduced for this purpose; in
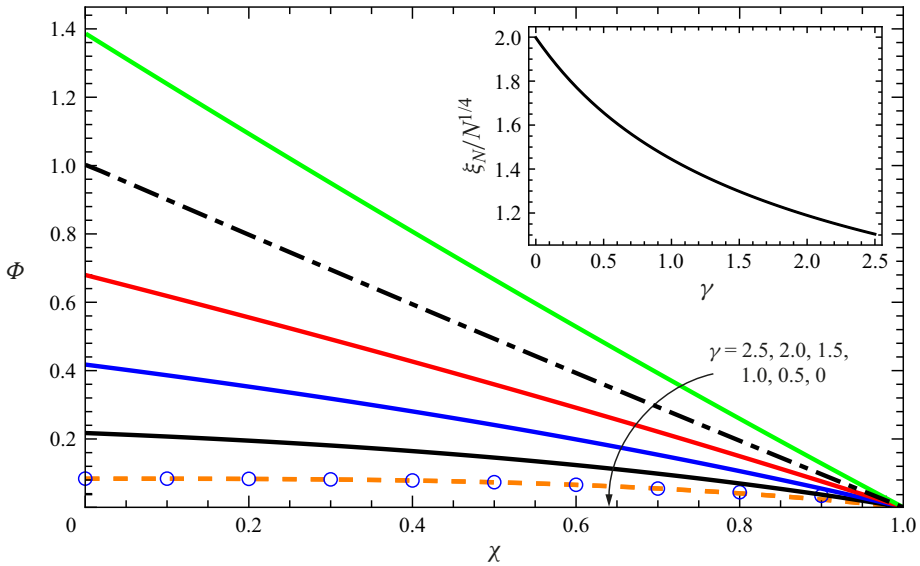
Figure 3. Self-similar solution for high local Forchheimer number, first-order approximation. For caption see figure 2. Open circles represent the analytical solution (3.27) for $\gamma = 0$.

particular, the shape factor is expanded in Taylor series about $\chi = 1$, finding

$$\Phi = \left(\frac{\gamma + 2}{4}\right)^2 (1 - \chi), \tag{3.28}$$

hence

$$\Phi'(1) = -\left(\frac{\gamma + 2}{4}\right)^2. \tag{3.29}$$

Figure 3 shows the shape function and the prefactor for different values of γ and N. The behaviour is quite similar to the functions shown in figure 2 for the low local Forchheimer number case.

For the general case $\gamma \neq 0$, the aspect ratio of the current (the ratio between its average thickness $\bar{H}$ and extent X_N) and its average slope are, respectively, (see Lauriola *et al.* 2018)

$$S \equiv \frac{\bar{H}}{X_N} = \frac{1}{N}\xi_N^2 T^{(\gamma-2)/2}\bar{\Phi}, \quad \overline{\left|\frac{\partial H}{\partial X}\right|} = \frac{1}{N}\xi_N^2 T^{(\gamma-2)/2}\overline{\left(\frac{d\Phi}{d\chi}\right)}, \tag{3.30a,b}$$

where the overline indicates the average value. Both quantities are functions of N via ξ_N and ϕ. In order to dispense with the average value of $\overline{(d\Phi/d\chi)}$, a different (crude) approximation for the average slope is reported in Appendix B, while Appendix C details the approach for deriving higher-order approximations of the similarity solution.

3.2.1. *The solution for $\gamma \to 2$ in the high-Forchheimer-number limit ($\zeta \gg 1$)*

With the same reasoning adopted in § 3.1.1, for $\zeta \gg 1$ the slope S and the speed U_N become

$$S = (\xi_N^2/N)\delta^{-1}, \quad U_N = \xi_N\delta^{-1/2}, \quad \xi_N = (2N)^{1/4}, \quad \text{for } \zeta \gg 1. \tag{3.31}$$

Again, larger values of q mean lower values of δ, resulting in a faster current of higher constant slope for increasing q.

3.3. *Values of local Forchheimer number*

Both local approximations examined, $\zeta = 4N|\partial H/\partial X| \ll 1$ or $\zeta = 4N|\partial H/\partial X| \gg 1$, may be appropriate for laboratory or field applications, depending on the fluids involved ($\Delta\rho$, ρ), the values of the porous medium properties (k, β) and the dimensionless head gradient, which varies over time. Typically, $N \in [10^{-5}, 10^{2}]$ as shown in Appendix A, while the order of magnitude of the average aspect ratio and average slope of the current may be deduced from (3.13a,b) or (3.30a,b) for low and high local Forchheimer number, respectively. Noteworthy, average aspect ratio and average slope differ only by a prefactor. If one considers values of average slope of order ϵ or less as required by the thin current approximation, (3.13a,b) and (3.30a,b), or their counterpart as reported in Appendix B, can be used to infer the time limit for the thin current approximation to be valid as a function of ϵ.

For $\gamma < 2$, the aspect ratio and the average slope decay with time, which means that the model of a thin long current is correct and that whatever the value of N, the local Forchheimer number ζ becomes asymptotically small, guaranteeing that the solution of the governing equations represented by (3.8)–(3.9) is the correct one in the long run.

For $\gamma > 2$, the $\zeta \gg 1$ hypothesis is certainly satisfied in the long run, since the average current slope increases over time. However, this may invalidate the thin current hypothesis. Therefore, only large values of N guarantee the validity of the results obtained by solving the governing equations ((3.25)–(3.26)) for a limited time interval, when the current slope is still modest and the local Forchheimer number is already high.

4. Solutions for $\gamma = 2$

This case has some practical interest as it corresponds to a linearly increasing flow rate. It is seen that for $\gamma = 2$, the time scale t_0 is no longer valid and this case can be treated defining an arbitrary time scale $\widetilde{t_0}$ and a new space scale $\widetilde{x_0} = (q/\phi)^{1/2}\widetilde{t_0}$, which arises from the integral constraint in (2.14a,b). In the following, a justification of an arbitrary time scale is given. Dimensionless variables thus become $\tilde{X} = x/\widetilde{x_0}$, $\tilde{X}_N = x_N/\widetilde{x_0}$, $\tilde{T} = t/\widetilde{t_0}$, $\tilde{H} = h/\widetilde{x_0}$. In the new dimensionless variables the governing equations become

$$\frac{\partial \tilde{H}}{\partial \tilde{T}} = -\frac{\delta}{2}\frac{\partial}{\partial \tilde{X}}\left[\tilde{H}\left(\sqrt{1 - 4N\frac{\partial \tilde{H}}{\partial \tilde{X}}} - 1\right)\right], \tag{4.1}$$

$$\int_0^{\tilde{X}_N} \tilde{H}\,\mathrm{d}\tilde{X} = \tilde{T}^2, \quad \tilde{H}(\tilde{X}_N(\tilde{T}), \tilde{T}) = 0, \tag{4.2}$$

where

$$\delta = \frac{u_0 \widetilde{t_0}}{\widetilde{x_0}} \equiv \frac{u_0}{(q/\phi)^{1/2}} \equiv \frac{\nu}{k\beta(q\phi)^{1/2}}. \tag{4.3}$$

We seek a self-similar solution of the form $\tilde{H} = N^{-1}\tilde{T}\Phi(\tilde{\xi})$, where $\tilde{\xi} = \tilde{X}/\tilde{T}$. Substituting into (4.1)–(4.2) yields

$$\frac{\delta}{2}\left[\Phi\left(\sqrt{1 - 4\Phi'} - 1\right)\right]' - \tilde{\xi}\Phi' + \Phi = 0, \tag{4.4}$$

$$\frac{1}{N} \int_0^{\tilde{\xi}_N} \Phi(\tilde{\xi}) \, d\tilde{\xi} = 1, \quad \Phi(\tilde{\xi}_N) = 0. \tag{4.5}$$

A simple solution to the above problem is a linear profile with $\Phi(\tilde{\xi}) = A(\tilde{\xi}_N - \tilde{\xi})$ where $A > 0$ and $\tilde{\xi}_N > 0$ are constants that can be computed by substitution into (4.4)–(4.5), obtaining the nonlinear system of equations

$$\tilde{\xi}_N = \frac{\delta}{2} \left(\sqrt{1 + 4A} - 1 \right), \quad \tilde{\xi}_N = \sqrt{\frac{2N}{A}} \tag{4.6}$$

in the unknowns $\tilde{\xi}_N$ and A.

The solution reads

$$\tilde{H}(\tilde{X}, \tilde{T}) = \frac{A}{N} \tilde{\xi}_N \tilde{T} \left(1 - \frac{\tilde{X}}{\tilde{\xi}_N \tilde{T}} \right), \tag{4.7}$$

with the nose position $\tilde{X}_N = \tilde{\xi}_N \tilde{T}$ and with a constant uniform slope equal to $S = |\partial \tilde{H}/\partial \tilde{X}| \equiv A/N$.

The existence of this particular self-similar solution can be predicted according to the reasoning reported in Appendix C.

A simpler reasoning indicates that the predicted GC is a wedge of constant slope S (see also Moutsopoulos 2009), with the nose propagating with constant speed U_N, both functions of N and δ only. Since the shape of the current and the speed are time independent, our selection of an arbitrary time scale is justified. In fact, in dimensional variables, the volume of fluid stored in the wedge is

$$\frac{1}{2} \phi x_N^2 S = q t^2. \tag{4.8}$$

Since the speed is constant, it follows $x_N = u_N t$, hence

$$\frac{1}{2} u_N^2 S = \frac{q}{\phi}, \tag{4.9}$$

or

$$U_N^2 S = 2 \left(\frac{q}{\phi u_0^2} \right) \equiv \frac{2}{\delta^2} \rightarrow U_N = \frac{1}{\delta} \sqrt{\frac{2}{S}} \equiv \frac{1}{\delta} \sqrt{\frac{2N}{A}}, \tag{4.10}$$

where U_N is scaled with u_0.

Figure 4 shows the slope of the current for $\gamma = 2$ and the constant speed U_N for increasing N (corresponding to increasing ζ). The red and blue curves, corresponding to $\delta = 1, 2$, respectively, reach the theoretical limits for low and high Forchheimer number, as computed in § 4.1 and in § 4.2, respectively.

4.1. *Low local Forchheimer number ($\zeta \ll 1$)*

For the low local Forchheimer number case ($\zeta \ll 1$), it results in $(\sqrt{1 - 4\Phi'} - 1) \approx -2\Phi'$ and (4.4) becomes

$$\delta \left(\Phi \Phi' \right)' + \tilde{\xi} \Phi' - \Phi = 0. \tag{4.11}$$

Equation (4.11) with the constraints (4.5) admits the following linear profile of the function Φ:

$$\Phi = \frac{2N}{\tilde{\xi}_N^2} \left(\tilde{\xi}_N - \tilde{\xi} \right), \quad \tilde{\xi}_N = (2N\delta)^{1/3}, \tag{4.12}$$
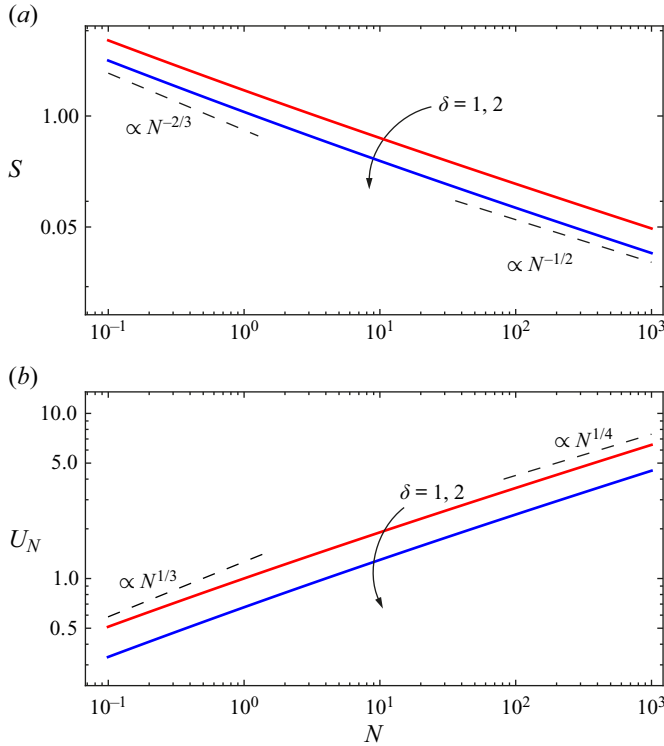
Figure 4. Analytical solution for $\gamma = 2$. (*a*) The uniform slope of the current S and (*b*) the nose speed U_N, for $\delta = 1, 2$. The dashed lines refer to the asymptotic values for low and large ζ.

and

$$\tilde{H}(\tilde{X}, \tilde{T}) = \frac{2}{\tilde{\xi}_N^2}\tilde{T}\left(\tilde{\xi}_N - \frac{\tilde{X}}{\tilde{T}}\right), \quad \text{with } \tilde{X}_N = \tilde{\xi}_N\tilde{T}. \tag{4.13}$$

The uniform slope S and speed U_N are

$$S = \frac{2}{(2N\delta)^{2/3}} \propto N^{-2/3}, \quad U_N \equiv \frac{1}{\delta}\sqrt{\frac{2}{S}} = (2N)^{1/3}\delta^{-2/3} \propto N^{1/3}, \tag{4.14}$$

corresponding to the results in (3.16).

4.2. *High local Forchheimer number* ($\zeta \gg 1$)

For the high local Forchheimer number case ($\zeta \gg 1$), it results ($\sqrt{1 - 4\Phi'} - 1) \approx 2\sqrt{-\Phi'}$ and (4.4) becomes

$$\delta\left(\Phi\left(-\Phi'\right)^{1/2}\right)' - \tilde{\xi}\Phi' + \Phi = 0. \tag{4.15}$$

The solution is the following linear profile of the function ϕ:

$$\phi = \frac{\tilde{\xi}_N^2}{\delta^2}\left(\tilde{\xi}_N - \tilde{\xi}\right), \quad \tilde{\xi}_N = (2N\delta^2)^{1/4}, \tag{4.16}$$

1000 A89-15

and

$$\tilde{H}(\tilde{X}, \tilde{T}) = \frac{2}{\tilde{\xi}_N^2} \tilde{T} \left(\tilde{\xi}_N - \frac{\tilde{X}}{\tilde{T}} \right), \quad \text{with } \tilde{X}_N = \tilde{\xi}_N \tilde{T}. \tag{4.17}$$

The uniform slope S and speed U_N are

$$S = \frac{2}{(2N\delta^2)^{1/2}} \propto N^{-1/2}, \quad U_N \equiv \frac{1}{\delta}\sqrt{\frac{2}{S}} = (2N)^{1/4}\delta^{-1/2} \propto N^{1/4}, \tag{4.18a,b}$$

corresponding to the results in (3.31).

5. Validation of approximate solutions with full numerical results

The numerical integration of (2.13) with constraints represented by (2.14a,b) is performed with a second-order two-stage explicit Runge–Kutta scheme, the improved Euler one (see e.g. Fletcher 1998). Variables are allocated at the knots of a uniform grid, staggering first derivatives in the midpoints. The initial condition is

$$H(X, 0) = a \left(\frac{X_{N0} - X}{X_{N0}} \right)^s \quad \text{for } \Delta X < X < X_{N0}, \tag{5.1}$$

where the coefficient a and the exponent s are dimensionless and X_{N0} is the initial nose position. The boundary condition at the origin represents the inflow rate per unit width, and reads

$$H(0, T)U(0, T) = \gamma T^{\gamma - 1}, \tag{5.2}$$

or

$$\frac{H\phi}{2} \left(-1 + \sqrt{1 + 4N \left| \frac{\partial H}{\partial X} \right|} \right) = \gamma T^{\gamma - 1}. \tag{5.3}$$

This condition is implemented in the predictor–corrector scheme by solving the nonlinear equation

$$\frac{(H_1 + H_2)\phi}{4} \left(-1 + \sqrt{1 + 4N \left| \frac{H_2 - H_1}{\Delta X} \right|} \right) = \gamma T^{\gamma - 1}, \tag{5.4}$$

where the unknown is $H_1 \equiv H(0, T)$ and $H_2 \equiv H(\Delta X, T - \Delta t)$. Grid-independent results were obtained with $\Delta X = 0.05$ and an initial $\Delta T = 10^{-6}$. For a smooth start of the integration process and to avoid numerical instabilities of the algorithm, it is convenient to select the parameters in (5.1) in order to approximately satisfy (5.4) with $T = \Delta T$. For most numerical simulations, the initial nose position is $X_{N0} = 0.05$, the exponent is $s = 0.3$ and the coefficient is $a = 0.5$.

Figure 5(a–c) show the computed profiles for $\gamma = 0$ and $N = 0.2, 5, 50$, also amenable to the analytical solution, representing a family of parabola. Figure 5(d–f) show the computed profiles for $N = 5$ and for increasing γ, with a waning, a constant and a waxing inflow rate, characterized by decreasing average slope of the profile and a constant uniform slope for $\gamma = 2$. The case $\gamma > 2$ (not shown) refers to time increasing average slope of the profile and accelerating nose speed.

Figures 6 and 7 show the nose position of the GC as a function of time. The two asymptotic values for low/high local Forchheimer numbers are also depicted. We notice that the condition $\gamma < 2$ leads to a more physically based GC, since the average slope
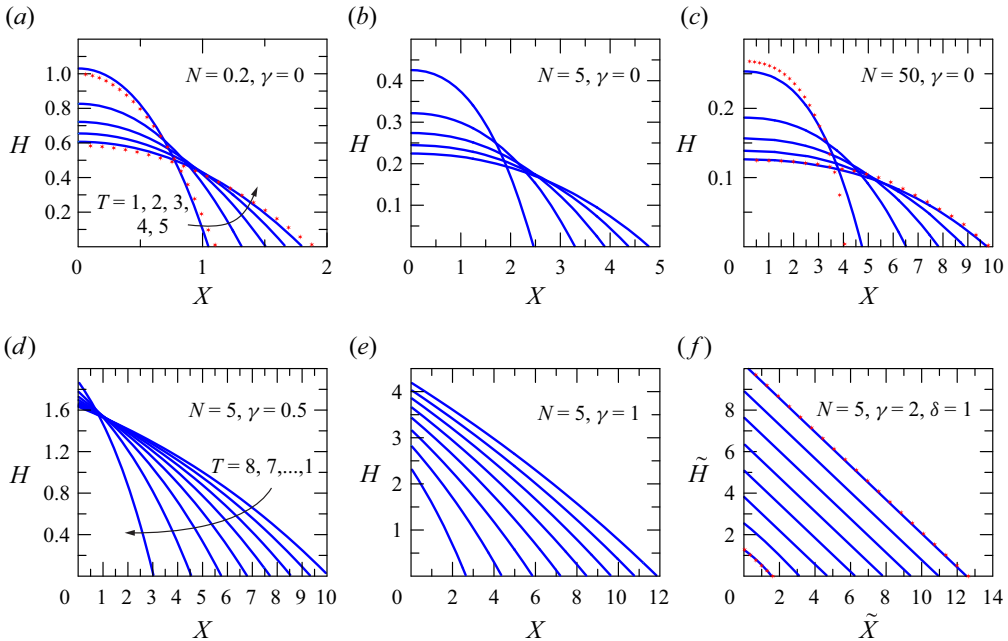
Figure 5. Numerical results for the time evolution of the profile of the GC with different values of the parameters N and γ, with $\phi = 0.3$. (*a–c*) Constant volume of fluid with increasing value of N; (*d*) waning current $\gamma = 0.5$; (*e*) constant inflow rate $\gamma = 1$; (*f*) waxing current with $\gamma = 2$, requiring a different scaling of the variables, computed for $\delta = 1$, also amenable to an analytical solution. Symbols are the analytical solution. For large values of γ the thin layer approximation is violated for extended periods of time.

of the profile decreases with time, preserving the shallow GC structure, as predicted by (3.13*a,b*), and sooner or later, also depending on the value of N, the local Forchheimer number becomes small. When $\gamma > 2$, the lower limit $X_N \sim T^{(\gamma+1)/3}$ predicts a faster nose than the upper limit $X_N \sim T^{(\gamma+2)/4}$, both with an accelerating nose speed; when $\gamma < 2$, the opposite is true, with a decelerating nose speed. For $\gamma = 2$, the two limits collapse, with a nose of the current advancing at constant speed. In contrast, the $\gamma > 2$ condition should drive the current towards the high local Forchheimer number limit, with $X_N \sim T^{(\gamma+2)/4}$, but with a progressive increase in the mean slope of the current profile that eventually undermines the thin GC model.

6. Experiments

6.1. *Experimental apparatus and protocol*

We performed multiple sets of experiments to corroborate our theoretical results. The main experiments were carried out in a polymethylmethacrylate-walled channel 6 cm wide and 150 cm long, filled with materials of a different nature to reproduce a wide range of porous media, see the schematic in figure 8. The inlet flows were injected by a vane pump with an electric motor having a speed controllable by an inverter, with the control signal generated by a personal computer through a data acquisition board; the same data acquisition board directly acquired the flow rate measured by a turbine transducer with a range of 0–250 ml s^{-1} and an accuracy of $\pm 0.4\%$ full scale. The maximum inflow rate was equal to 150 ml s^{-1}. The injected fluid was tap water with food colour added for a more effective visualization. The current profile was detected by a fixed video
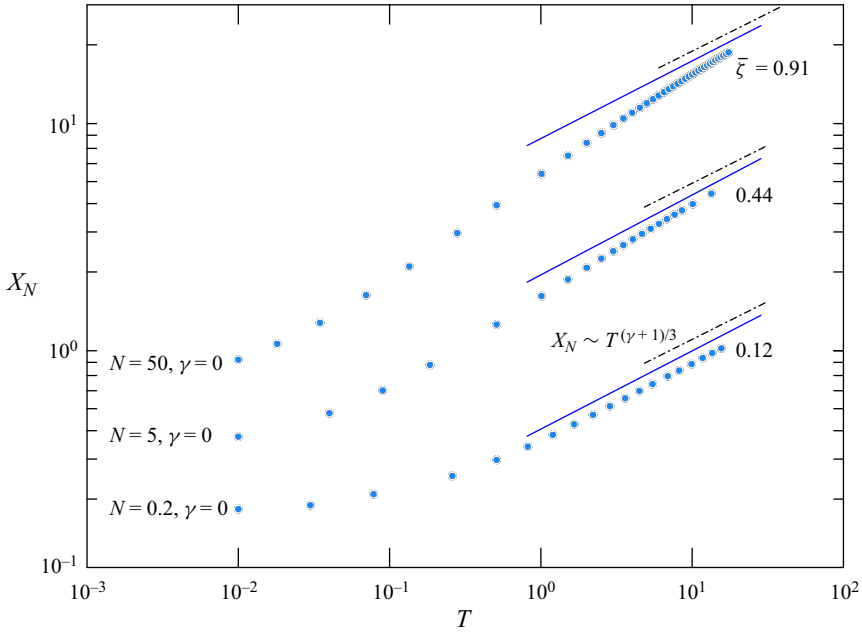
Figure 6. Time evolution of the nose position for GCs with different values of the parameter N and for $\gamma = 0$, $\phi = 0.3$, low local Forchheimer number. Symbols are the results of the numerical integration, the blue continuous lines are the interpolation of the late time nose coordinates, the dash–dotted black lines are the low local Forchheimer number asymptotes as provided by the self-similar solution (3.7a,b). The value of $\bar{\zeta}$ is averaged on the whole length of the GC and data are translated vertically for easier visualization.
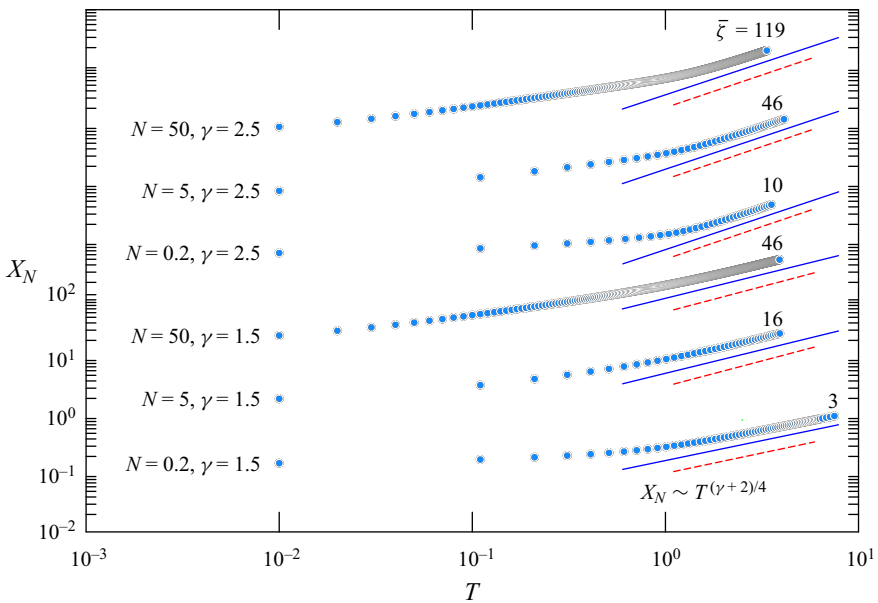

Figure 7. Time evolution of the nose position for GCs with different values of the parameter N and of the exponent γ, $\phi = 0.3$, high local Forchheimer number. Symbols are the results of the numerical integration, the blue continuous lines are the interpolation of the late time nose coordinates, the dashed red lines are the high local Forchheimer number asymptotes as provided by the self-similar solution (3.24a,b). The value of $\bar{\zeta}$ is averaged on the whole length of the GC and data are translated vertically for easier visualization.

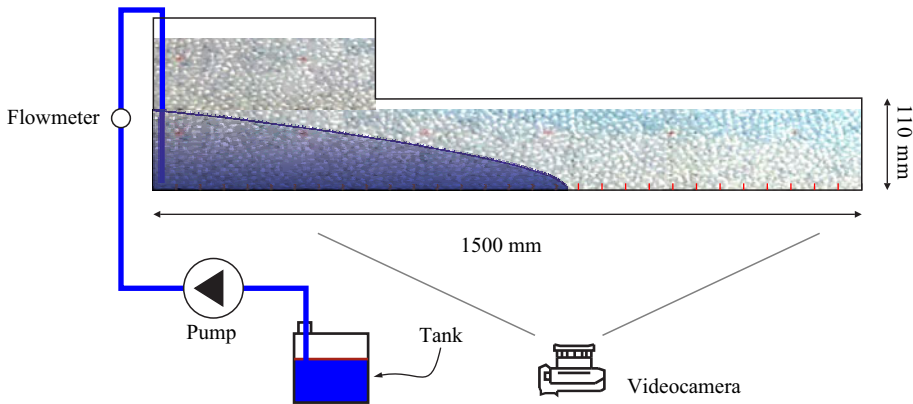Figure 8. Schematic of the channel filled with porous medium and of the instruments for injection and control of the flow rate.

camera at 3840×2160 pixels at 30 frames per second and by a similar mobile camera with close-up shots of the flow nose by a mobile operator. The geometric reference was provided by a transparent grid superimposed on the transparent vertical wall of the channel.

As a first step, we determined the two parameters α and β performing preliminary experiments using two additional experimental devices, identical in principle to the main one but having a different size in order to limit the boundary effects if large glass beads are used. A schematic of the two devices is shown in figure 9. Both are circular pipes filled with the porous medium and having an internal diameter D_{int} of 46 ± 1 mm or 102 ± 2 mm; the larger diameter was used when larger particles were employed for the porous medium. The pipe is fed by a controlled flow, with two pressure ports $l = 250$–350 ± 5 mm apart connected to a differential piezometer. In such a system, the head gradient is equal to $\Delta h/l$ and the Darcian velocity is equal to $4Q/(\pi D_{int}^2)$, where Δh is the head difference between the ports and Q the flow rate. Data were acquired with different Q values, with an overall accuracy of 4 % in the net pressure gradient $\Delta p/l = \rho g \Delta h/l$ and of 3 % in the Darcian velocity estimates. Figure 10 shows results, with the 95 % confidence limits, of the experimental evaluation of α and β for glass beads of uniform size having different diameters and for gravel. The confidence limits were computed by assuming a normal distribution of the experimental data and performing a Monte Carlo simulation with 10 000 data sets.

Sixteen experiments were performed with three different materials, i.e. glass spheres of diameter $d = 4.0 \pm 0.1$ mm, glass spheres of diameter $d = 15.5 \pm 0.3$ mm and natural marble gravel with particles in the range 7–15 mm. The time exponent γ is variable in the range 0.5–2.5, with only one superwaxing current test with $\gamma = 5.2$. Each experiment lasts between 20 and 35 s, depending on the input condition (exponent γ) and the hydraulic permeability of the porous medium. We deliberately discarded performing the constant volume tests ($\gamma = 0$) because the current would have decayed very quickly in a Darcy regime, even before settling into the Forchheimer self-similarity regime. The experiments were planned with various combinations of porous media and γ values; table 1 summarizes experiments and corresponding parameters. Sample snapshots of the current profile for Exp. 13 are shown in figure 11.
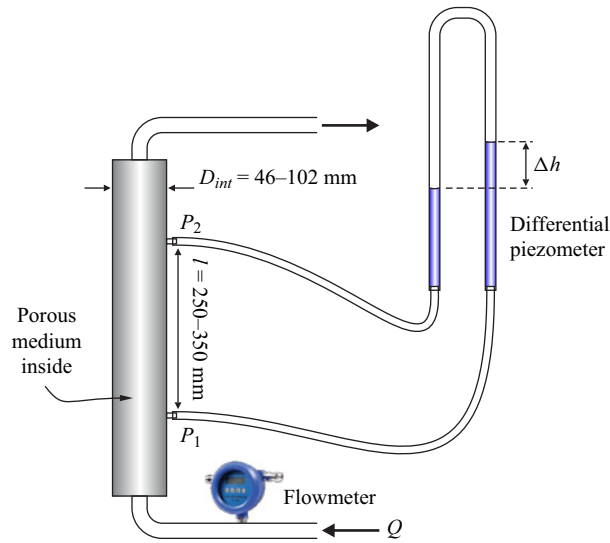
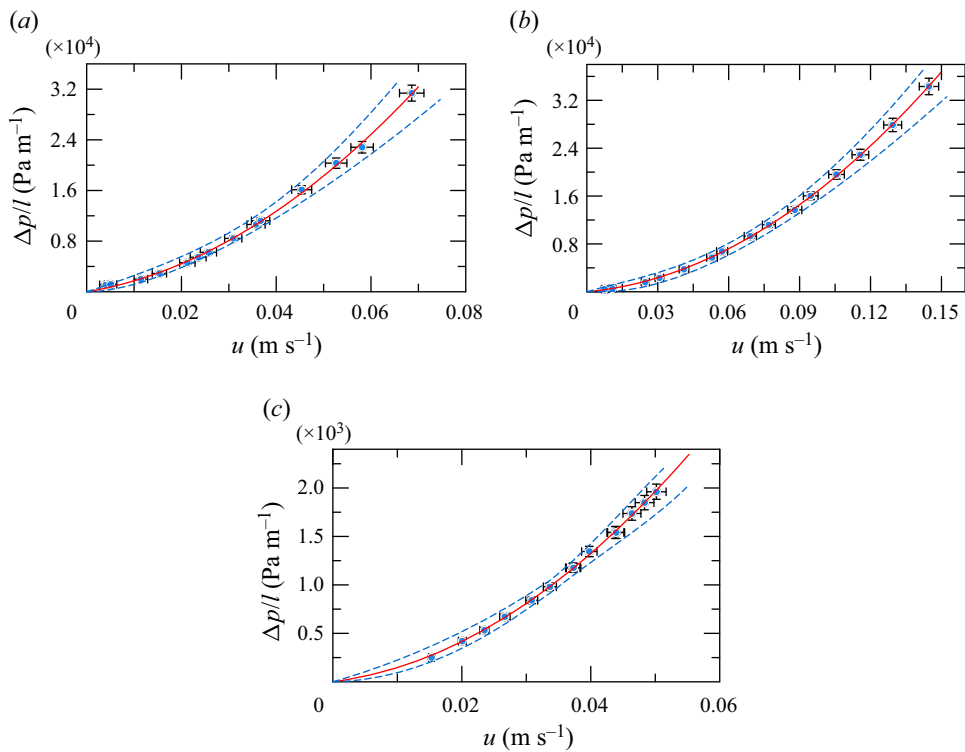Figure 9. Experimental device for estimating the Forchheimer's parameters α and β.

Figure 10. Experimental evaluation of the parameters α and β. (*a*) Glass beads $d = 4 \pm 0.1$ mm, (*b*) natural gravel 7–15 mm, (*c*) glass beads $d = 15.5 \pm 0.3$ mm. Symbols are measurements with the error bars, the continuous curves are the interpolating functions $\Delta p/l = \alpha u + \rho \beta u^2$ and the dashed curves are the 95 % confidence limits computed with a Monte Carlo simulation.

Exp.	d (mm)	ϕ (%)	γ	q (ml s$^{-\gamma}$)	α (Pa s m^{-2})	β (m^{-1})	N
(b)1	4.0 ± 0.1	38 ± 1	0.71	107.4	$1.28 \times 10^5 \pm 20\,\%$	$4760 \pm 13\,\%$	2.8
(b)2			1.00	53.4			
(b)3			1.00	59.6			
(b)4			1.00	80.0			
(b)5			2.00	0.69			
(b)6			2.30	0.44			
(B)7	15.5 ± 0.3	41 ± 1	0.50	233.3	$9.48 \times 10^3 \pm 25\,\%$	$590 \pm 11\,\%$	64.0
(B)8			0.70	184.7			
(B)9			1.00	138.3			
(B)10			2.00	6.50			
(B)11			2.50	2.24			
(g)12	$7–15$	38 ± 1	0.70	197.5	$3.89 \times 10^4 \pm 31\,\%$	$1370 \pm 10\,\%$	8.8
(g)13			1.00	109.0			
(g)14			2.00	5.53			
(g)15			2.00	6.89			
(g)16			5.20	4.43×10^{-5}			

Table 1. List of the experiments: (b) indicates smaller glass beads with $d = 4.0 \pm 0.1$ mm; (B) indicates larger glass beads with $d = 15.5 \pm 0.3$ mm; (g) indicates gravel with diameter $d = 7–15$ mm.
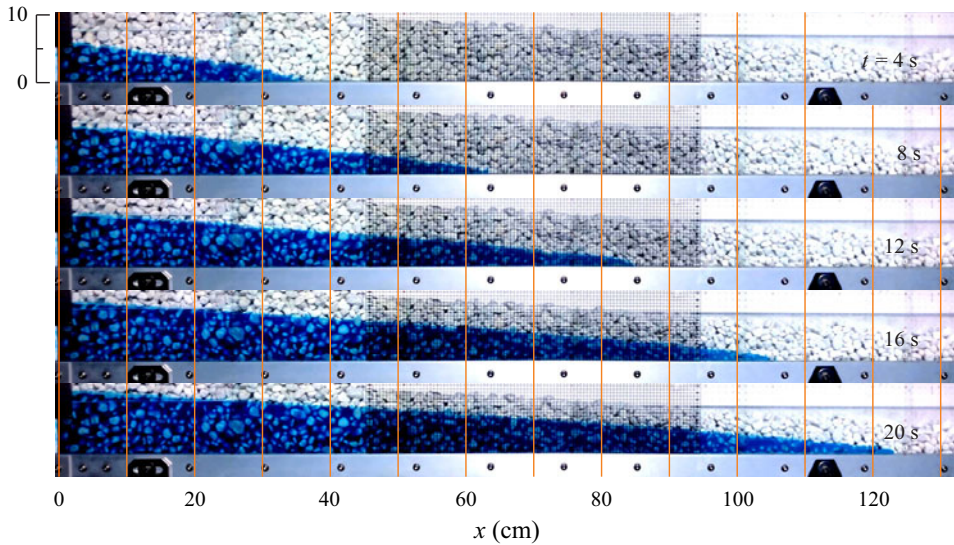

Figure 11. Snapshots of the profiles of the current for Exp. 13. Constant inflow rate with the current advancing in natural gravels.

6.2. *Experimental results and discussion*

Figure 12 shows the current profile for Exp. (b)5, with a linearly increasing inflow rate. The straight dash–dotted lines are the theory, which is in very good agreement with the experimental profiles. Similar good agreement is also found for other experiments (not shown).

Results for the nose position of the currents are shown in figure 13(*a*,*b*) for all experiments with a waxing or constant inflow rate ($\gamma \leq 1$). The graphs show, on a
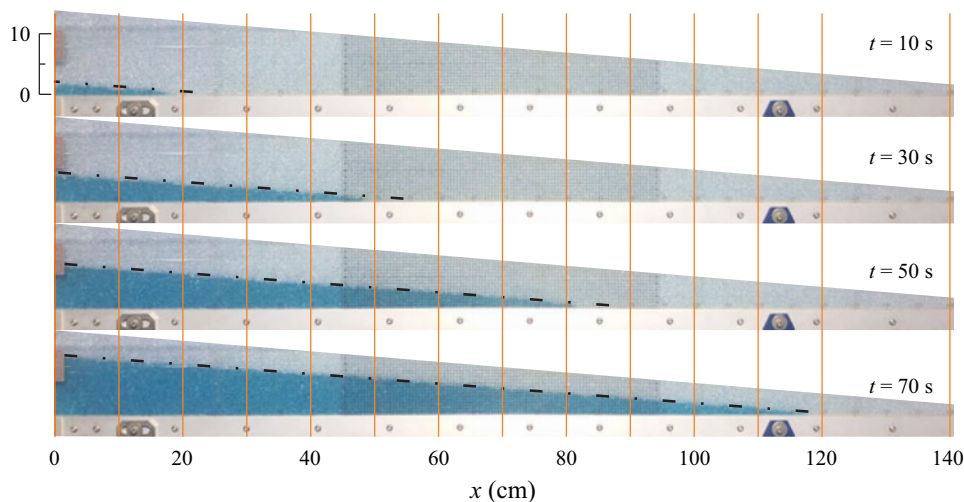
Figure 12. Profiles of the current for Exp. (b)5, small glass beads with linearly increasing inflow rate, $\gamma = 2$ and $X_N \propto T$. The dash–dotted straight lines are the theoretical results.

bilogarithmic scale, the dependency on time of the experimental nose position compared with its theoretical counterpart, calculated for the case of high/low local Forchheimer number, depending on the regime asymptotically reached by the GC. In seven instances, the current asymptotically reaches the high local Forchheimer regime, while for the remaining two cases (Exp. (B)9 and Exp. (g)13), a progressive deceleration of the nose is observed until the low local Forchheimer number regime is reached. It is seen that the results of the theoretical models are in good agreement with the experiments, i.e. the semianalytical predictions based on the approximation well predict the asymptotic behaviour of the current nose.

Figure 14(a) shows the nose position for the experiments with $\gamma = 2$, corresponding to a linearly increasing flow rate. In this case, the mathematical formulation admits an analytical solution predicting a constant nose speed. For a better comparison, a linear scale was used for both axes. After an initial adaptation, the self-similar regime clearly emerges, with experimental points aligned on a straight line, indicating a good match with theory. Figure 14(b), again using logarithmic scales, refers to waxing inflow rate tests with $\gamma > 2$. For Exp. 6 and Exp. 11 the asymptotic high local Forchheimer number regime is well reproduced, but for the superwaxing inflow rate Exp. 16 an evident acceleration of the nose is not followed by the limit high regime, which would imply $X_N \propto T^{1.8}$. This phenomenon is due to the fact that the maximum flow rate of the pump was reached before self-similarity was perfected. Noteworthy, this is a strongly accelerating flow: the GC has to travel a reasonable distance from the origin before it converges to self-similarity, forgetting the initial and boundary conditions. At the same time, when the inflow rate becomes constant as the pump reaches its maximum flow rate, the profile evolves towards the characteristic of $\gamma = 1$.

This analysis of the evolution of the regime of the current nose can be carried out by calculating the value of the local time exponent ω (where $X_N \propto T^\omega$) as $\omega = T\dot{X}_N/X_N$, interpolating the experimental data $X_N(T)$ with a polynomial and calculating the time derivative $\dot{X}_N$. Figure 15 shows the time evolution of ω for Exp. 2 with a constant inflow rate ($\gamma = 1$), with a lower/upper limit equal to 0.67/0.75, and for Exp. 16 in superwaxing inflow rate ($\gamma = 5.2$). For Exp. 2, after an initial adjustment, ω reaches a plateau around
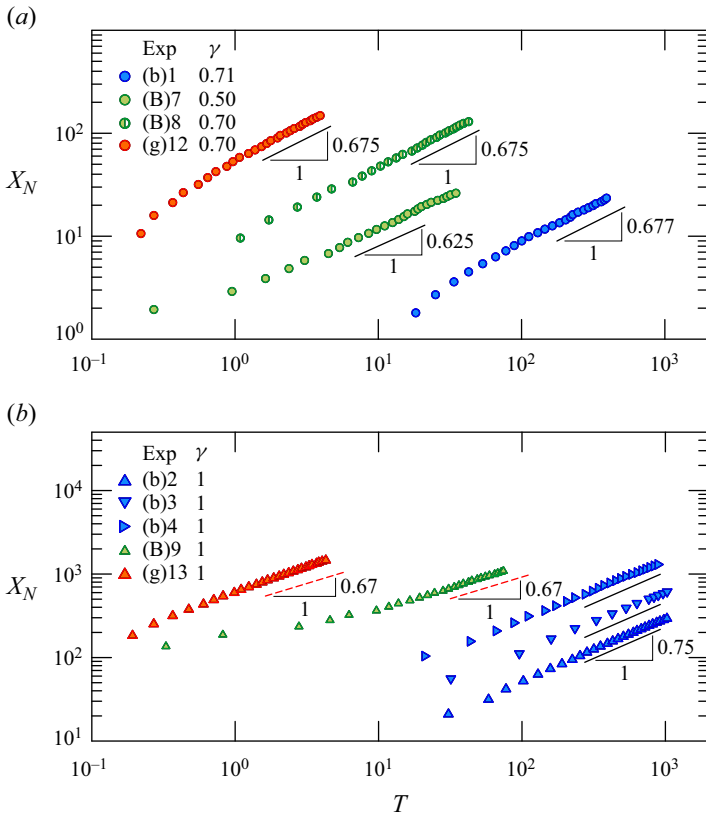
Figure 13. Experimental nose position X_N versus time T. (*a*) Waning inflow rate with different values of γ, and (*b*) constant inflow rate with $\gamma = 1$. The continuous black and dashed red lines refer to the high/low local Forchheimer number regime, with a time exponent equal to $(\gamma + 2)/4$ (high) and $(\gamma + 1)/3$ (low), respectively. Data are translated along the vertical for better visualization.

0.75, followed by a progressive decay towards the low limit regime $\omega = 0.67$. For Exp. 16, there is an evident acceleration with a maximum $\omega \approx 1.28$, followed by a decay when the pump has reached the maximum inflow rate.

7. Summary and conclusions

The present study extends the well-known problem of GC propagation in porous media to the Forchheimer regime. The starting assumptions are (i) plane GCs advancing in homogeneous porous media over an impermeable bottom under the Darcy–Forchheimer flow law; (ii) thin current warranting the lubrication approximation; (iii) lack of capillary effects; (iv) existence of a representative elementary volume even in presence of coarse media. Further, the model assumes that the fluid volume of the current varies with time according to a power function of exponent γ, capable of simulating the dam-break condition ($\gamma = 0$), constant, waxing and waning inflow rates.

The study adopts analytical, numerical and experimental approaches. Mathematically, the resulting nonlinear, diffusion-like governing equations in $H(X, T)$ requires, in general, a numerical approach. However, it is possible to find certain self-similar solutions that transform the PDE describing the propagation of the current into an easily solved ODE
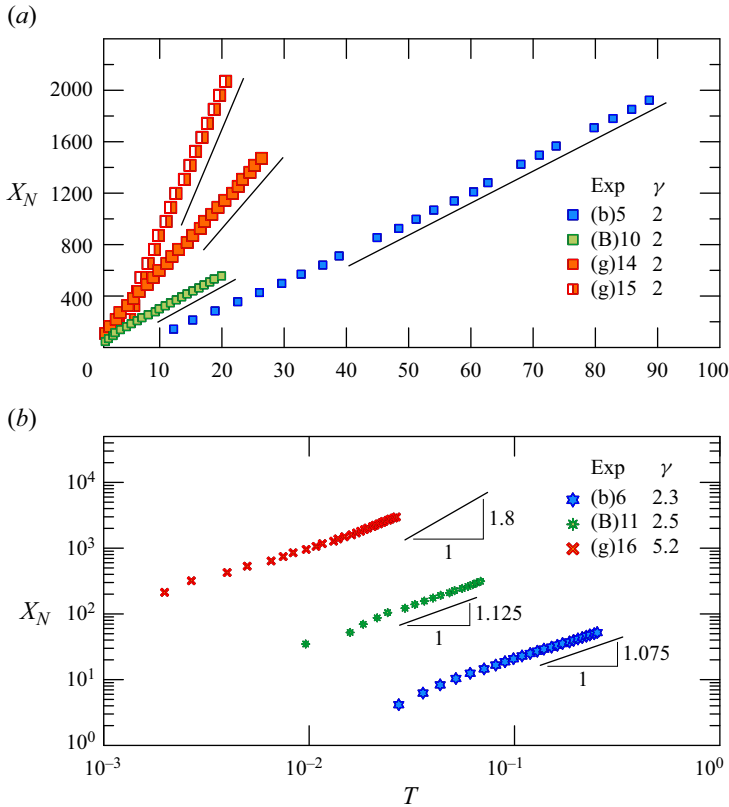
Figure 14. Experimental nose position X_N versus time T. (*a*) Waxing inflow rate with $\gamma = 2$, and (*b*) waxing inflow rate with $\gamma > 2$. Panel (*a*) axes are linear for stricter validation. For caption, see figure 13.
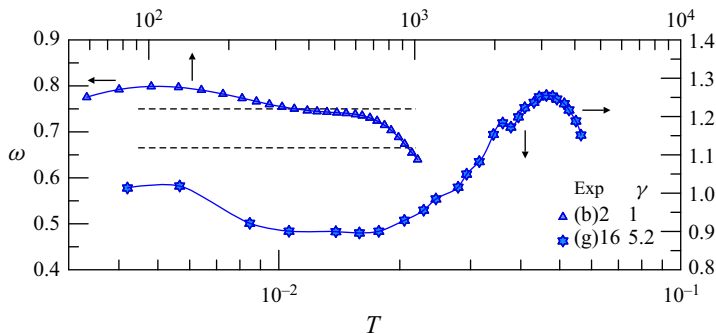

Figure 15. Local time exponent ω of the nose position, with $X_N \propto T^{\omega}$. The dashed lines are the theoretical values $\omega = 0.75$ for $\bar{\zeta} \gg 1$ (upper line) and $\omega = 0.67$ for $\bar{\zeta} \ll 1$ (lower line) and Exp. (b)2 with $\gamma = 1$. The arrows indicate the axes for the two (upper and lower) lines, time increases from left to right.

in $H(\chi)$, where χ combines space X and time T, eliminating the initial condition and transforming the boundary condition at the origin into an integral mass conservation of the fluid over time. The ODE numerical solution is valid in the intermediate asymptotic regime and does not require an initial condition, as a consequence of the reduction of the number of the independent variables. Specifically, self-similar solutions are obtained in

the limiting conditions of a local Forchheimer number very small/large at first/zero order, respectively. As subcases, analytical solutions were obtained for $\gamma = 0$ and for $\gamma = 2$. This last condition is obtained either with governing equations written with a different scaling of the time, or as a limit for $\gamma \to 2$ of the governing equations written with the standard scaling adopted for $\gamma \neq 2$. The results are obviously the same. Table 2 summarizes the approaches adopted to solve the governing equations and some main results.

The asymptotic behaviour of the self-similar solutions has been numerically verified by comparison with the numerical results of the direct integration of the full governing equations. Although the robustness of the adopted schemes suggests that the proposed solutions are capable of reproducing physical reality, experimental validation is essential.

A series of 16 experiments carried out in a channel filled with glass spheres of two different diameters and natural marble gravel allowed the recording of the temporal position of the nose and the profiles of the currents under waning, constant and waxing inflow rate. The two coefficients α and β were estimated for the three different porous media with a different experimental apparatus. The data analysis shows that within the limits of the uncertainties the theoretical model is in good agreement with the experimental evidence, and confirms the existence of self-similar regimes under Darcy–Forchheimer flow.

Further conclusions specific to different values of γ are as follows.

(i) For $\gamma < 1$ (waning inflow rate) in the high-Forchheimer-number regime, the local Forchheimer number decreases asymptotically as the average current slope slows down as $\sim T^{(\gamma-2)/2}$. This means that flows initially in the high-Forchheimer-number regime asymptotically reach the low-Forchheimer number-regime. In particular, for the dam break case ($\gamma = 0$), the profile evolves from a cubic to a quadratic parabola, and the nose propagation rate goes from $\sim T^{1/2}$ to $\sim T^{1/3}$. This behaviour also applies to GC in the waxing regime, but with $\gamma < 2$, i.e. GCs with decelerating nose speed.

(ii) For $\gamma = 2$ (input flow rate increasing linearly with time), the problem admits a self-similar solution with a linear profile and the nose advances at constant speed. This solution is similar to that obtained for a GC of Herschel–Bulkley fluid by Di Federico *et al.* (2017). The two low/high local Forchheimer number subcases fall into the general case, with some simplifications. Note that the slope of the current profile is both time-invariant and uniform, hence, the current will not change its average local Forchheimer number over time. The current midplane section is a triangle with homothetic transformation during time.

(iii) For $\gamma > 2$, even if the GC is initially in the low-Forchheimer-number regime, it evolves towards the high-Forchheimer number-regime as the average slope of the profile grows over time. However, before reaching this regime, the average slope may assume such large values that the thin current model becomes inapplicable. Hence, there is an intermediate interval when both events occur, rendering the high-Forchheimer-number regime feasible.

Finally, the appendices illustrate specific aspects of the problem at hand. Appendix A illustrates different possible expressions for the pure parameter N governing the dimensionless formulations of the problem. Here N is shown to be proportional to the intensity of the nonlinear Forchheimer correction and to the squared ratio between buoyancy and viscous forces, akin to a Grashof number. Here N ranges normally between 10^{-5} and 10^2 and between 2.8 and 64 in our experiments.

		$\gamma \neq 2$			
		H	X_N	ξ_N	$\bar{\zeta}$	$\Phi'(1)$
		finite difference X, T code is required				
$\forall\zeta$						
$\zeta \ll 1$	self-sim. num. int. in χ	$\xi_N^2 N^{-1} T^{(2\gamma-1)/3}\Phi(\chi)$	$\xi_N T^{(\gamma+1)/3}$	$(N^{-1}\int_0^1 \Phi\,\mathrm{d}\chi)^{-1/3}$	$\Phi(0)\dfrac{4\xi_N}{T^{(2-\gamma)/3}}$	$-(\gamma+1)/3$
	analytical if $\gamma=0$	$\dfrac{3^{1/3}}{2N^{1/3}T^{1/3}}(1-\chi^2)$	$(9N)^{1/3}T^{1/3}$	$(9N)^{1/3}$	$\dfrac{2N^{1/3}}{3^{1/3}T^{2/3}}$	—
$\zeta \gg 1$	self-sim. num. int. in χ	$\xi_N^3 N^{-1} T^{(3\gamma-2)/4}\Phi(\chi)$	$\xi_N T^{(\gamma+2)/4}$	$(N^{-1}\int_0^1 \Phi\,\mathrm{d}\chi)^{-1/4}$	$\Phi(0)\dfrac{4\xi_N^2}{T^{(2-\gamma)/2}}$	$-(\gamma+2)/4$
	analytical if $\gamma=0$	$\dfrac{2}{3N^{1/4}T^{1/2}}(1-\chi^3)$	$2N^{1/4}\sqrt{T}$	$2N^{1/4}$	$\dfrac{4\sqrt{N}}{3T}$	—
		$\gamma=2$, self-similar analytical solution				
		$\tilde{H}$	$\tilde{X}_N$	A	ξ_N	$\bar{\zeta}$
$\forall\zeta$		$A\xi_N\tilde{T}(1-\tilde{\chi})$	$\xi_N\tilde{T}$	A	$\begin{cases}\xi_N=\dfrac{\delta}{2}\left(\sqrt{1+4A}-1\right)\\[4pt]\xi_N=\sqrt{\dfrac{2N}{A}}\end{cases}$	ξ_N
$\zeta \ll 1$		$\dfrac{2^{2/3}}{(N\delta)^{1/3}}\tilde{T}(1-\tilde{\chi})$	$(2N\delta)^{1/3}\tilde{T}$	$\dfrac{2^{1/3}}{(N\delta)^{2/3}}$	$(2N\delta)^{1/3}$	$\dfrac{2^{7/3}N}{(N\delta)^{2/3}}$
$\zeta \gg 1$		$\dfrac{2^{3/4}}{\sqrt{\delta}\sqrt{N}}\tilde{T}(1-\tilde{\chi})$	$(2N)^{1/4}\sqrt{\delta\tilde{T}}$	$\dfrac{\sqrt{2}}{\delta\sqrt{N}}$	$(2N)^{1/4}\sqrt{\delta}$	$\dfrac{4\sqrt{2N}}{\delta}$

Table 2. Summary of the methods adopted for solving the governing equations. Here $\bar{\zeta}=(4N/X_N)\int_0^{X_N}|\partial H/\partial X|\,\mathrm{d}X$ is the (average) local Forchheimer number, $\Phi'(1)$ is the second boundary condition for the numerical integration of the governing equations admitting a self-similar solution. The solution for $\gamma=2$ can be also obtained as limit for $\gamma\to 2$ of the solution for $\gamma\neq 2$, see the details in the main body of the text.

Appendix B presents a simple expression for the average slope of the current.

In Appendix C the self-similar solution approach is briefly derived and a self-similar solution of the general case is sketched, with the expansion in series of functions where the fundamental solution corresponds to the low local Forchheimer number case at first order. The coefficients of the series are powers of time calculated to guarantee the invariance of the additional terms in the same parameter of transformations that admits the self-similarity of the fundamental solution. The convergence condition of the function series indicates that, at each order, the solution is valid if $T \ll T_c \equiv N^{3/(2-\gamma)}$ when $\gamma < 2$ and $T \gg T_c$ when $\gamma > 2$. T_c is named critical time. For $\gamma = 2$ the value of $T_c \to \infty$ and this suggests that the self-similar solution is possible for the complete governing equations, as actually verified.

Future developments include the extension of the Darcy–Forchheimer flow law to infinite radial geometry, finite domains and non-Newtonian flows.

Declaration of interests. The authors report no conflict of interest.

Author ORCIDs.

Luca Chiapponi https://orcid.org/0000-0002-0621-788X;

Sandro Longo https://orcid.org/0000-0003-1212-0686;

Vittorio Di Federico https://orcid.org/0000-0001-9554-0373.

Appendix A. The dimensionless parameter N

The pure number N may be expressed as a function of well-known dimensionless parameters in fluid mechanics (see e.g. Massey 1971; Longo 2021*a*). Multiplying and dividing (2.15) by $u_0^2 d^2$, where u_0 is the velocity scale defined in (2.11*a–c*) and d the characteristic length (diameter) of the porous medium, yields

$$N = \frac{Re\,Fo\,Da}{Fr_d^2}, \tag{A1}$$

where $Re = (\rho u_0 d)/\mu$ is the classical pore-scale Reynolds number, equal to the ratio between convective inertial forces and viscous forces, $Fo = (\rho \beta k u_0)/\mu$ is the Forchheimer number, a modified version of the Reynolds number expressing the ratio between nonlinear effects associated with the Forchheimer correction to Darcy's law and viscous effects, $Da = k/d^2$ is the Darcy number, representing the relative effect of the permeability of the medium versus its cross-sectional area and $Fr_d = u_0/\sqrt{(\Delta \rho/\rho)gd}$ a pore-scale densimetric Froude number, equal to the square root of the ratio between convective inertia and buoyancy.

Note that (A1) can be recast as

$$N = \frac{d^2}{h_0^2} \frac{Re'\,Fo\,Da}{Fr_d'^2} \tag{A2}$$

upon redefining the pore-scale Reynolds and densimetric Froude numbers via their large-scale counterparts $Re' = (\rho u_0 h_0)/\mu$, $Fr'_d = u_0/\sqrt{(\Delta\rho/\rho)gh_0}$, where the height of the porous domain h_0 is taken as the relevant length scale *in lieu* of the characteristic pore diameter d.

A third, and more parsimonious, option to represent N is writing

$$N = \frac{Re'' Fo}{Fr''^2_d}, \tag{A3}$$

where the alternative definitions of the Reynolds number $Re'' = (\rho u_0 \sqrt{k})/\mu$ and densimetric Froude number $Fr''_d = u_0/\sqrt{(\Delta\rho/\rho)g\sqrt{k}}$ incorporate $\sqrt{k}$ as the relevant length scale.

Finally, an alternative expression of (A3) that dispenses with the Forchheimer number is

$$N = C_D \frac{Re''^2}{Fr''^2_d} \propto \left(\frac{\text{buoyancy forces}}{\text{viscous forces}}\right)^2, \tag{A4}$$

where C_D is the dimensionless form-drag coefficient defined in (2.2). Equation (A4) demonstrates that essentially N is a Grashof number modulated by the dimensionless factor C_D expressing the intensity of the Forchheimer nonlinear correction to Darcy's law. In fact, the Grashof number is usually expressed as

$$Gr = \frac{\Delta\rho}{\rho} \frac{gl^3}{\nu^2}, \tag{A5}$$

where l is a length scale. Here, the density variations are not linked to temperature effects as usual, but to the presence of two fluids, the intruding and the ambient, having a density difference $\Delta\rho$. When l is taken to be equal to $\sqrt{k}$ and using (2.2), it is seen that $N = C_D Gr$.

To derive values of N typical of laboratory or field applications, consider first a $\Delta\rho/\rho$ in the range $0.1 - 0.9$, the two bounds being representative of the Boussinesq or non-Boussinesq regime, respectively. Then, one can typically take for the fluid properties those of water at $10\,^{\circ}$C, $\rho = 999.7\,\text{kg m}^{-3}$ and $\mu = 1.337 \times 10^{-3}\,\text{Pa s}$. As β and k are correlated (Lenci *et al.* 2022), ranges of values of k and β are conveniently deduced from Sidiropoulou, Moutsopoulos & Tsihrintzis (2007), who report k and b pairs ($\beta = b/g$) as a consequence of (2.1) and (2.3) measured in different experiments. There, we select the experiment on sand media with the lowest k and that on gravel media with the highest k as ideally representative of the two approximate regimes of low and high local Forchheimer number. The corresponding parameter values are $k = 2.1 \times 10^{-10}\,\text{m}^2$, $\beta = 759\,\text{m}^{-1}$ for sand (their data set #77), and $k = 2.04 \times 10^{-6}\,\text{m}^2$, $\beta = 50\,\text{m}^{-1}$ for gravel (their data set #72). These two pairs yield $N = 1.84 \times 10^{-5}$ or $N = 1.65 \times 10^{-4}$ for sand and $N = 3.49$ or $N = 31.4$ for gravel, depending whether $\Delta\rho/\rho = 0.1$ or $\Delta\rho/\rho = 0.9$. Hence the potential range of N is very large, i.e. approximately $N \in [10^{-5}, 10^2]$ for fluids with a kinematic viscosity close to water, and includes the case $N = 1$ entailing roughly a balance between buoyancy and viscous forces. Most fluids have a kinematic viscosity higher than water, so in these cases the lower limit decreases below 10^{-5}; it can (modestly) increase above 10^2 for those few fluids having kinematic viscosity lower than water. In the experiments described in § 6, the value of N ranges between 2.8 and 64.

Appendix B. An alternative expression for the average slope of the current

An alternative, approximate expression for the slope of the GC is derived here, to dispense with the evaluation of the average value of the first derivative of the shape function, $\overline{d\Phi/d\chi}$, in (3.13*a,b*) and (3.30*a,b*). Approximating the current with a prism of longitudinal triangular cross-section of length x_N and height $x_N \tan\varphi$, where $\tan\varphi$ is the slope, the current volume per unit width is $\frac{1}{2}x_N^2 \tan\varphi = qt^\gamma/\phi$, or $\frac{1}{2}X_N^2 \tan\varphi = T^\gamma$ in dimensionless form, yielding $\tan\varphi = |\partial H/\partial X| = (2T^\gamma)/X_N^2$. This gives for the slope of the current

$$S \equiv \left|\frac{\partial H}{\partial X}\right| = \frac{2}{\xi_N^2}T^{(\gamma-2)/3}, \quad S \equiv \left|\frac{\partial H}{\partial X}\right| = \frac{2}{\xi_N^2}T^{(\gamma-2)/2} \qquad \text{(B1a,b)}$$

for the low- and high-Forchheimer case, respectively.

The approximation is exact if $\gamma = 2$ and, in this case, the current profile is linear, but the slope must be computed with the same approach adopted for (3.16)–(3.31).

Appendix C. The self-similar solution approach and the solution expanding in series of functions

We first consider the reduced problem in the limit $\zeta \ll 1$, see (3.3) with the constraints (2.14*a,b*). The transformation group leaving the problem invariant can be obtained by assuming a possible structure as $X' = aX, T' = bT, H' = cH$, where the prime refers to the variable in a new space and a, b, c are real coefficients. Substituting into the governing equations yields

$$\frac{\partial H'}{\partial T'} = N\frac{\partial}{\partial X'}\left(H'\frac{\partial H'}{\partial X'}\right) \rightarrow \frac{c}{b}\frac{\partial H}{\partial T} = N\frac{c^2}{b^2}\frac{\partial}{\partial X}\left(H\frac{\partial H}{\partial X}\right), \qquad \text{(C1)}$$

and

$$\int_0^\infty H'\,dX' = T'^\gamma \rightarrow ac\int_0^\infty H\,dX = b^\gamma T^\gamma. \qquad \text{(C2)}$$

The invariance requires that

$$\frac{c}{b} = \frac{c^2}{b^2}, \quad ac = b^\gamma, \qquad \text{(C3)}$$

which admits the solution

$$b = a^{F_2}, c = a^{F_1}, \quad \text{with } F_1 = \frac{2\gamma - 1}{\gamma + 1}, F_2 = 2 - F_1. \qquad \text{(C4)}$$

That means that the group of transformation for the single-parameter a reads

$$X' = aX, \quad T' = a^{F_2}T, \quad H' = a^{F_1}H. \qquad \text{(C5a–c)}$$

Assuming time as fundamental variable, the dimensions of X and H are $X \sim T^{-r}$ and $H \sim T^{-s}$ with $r = 1/F_2$ and $s = F_1/F_2$. According to the principle of covariance, the solution of the governing equations can be expressed as $f(HT^{-s}, XT^{-r}) = 0$. For progress, we can assume that $H = T^s f(XT^{-r})$. This is the conceptualization that leads to the governing equations represented by (3.8)–(3.9).

Looking at the full governing equations ((2.13)–($2.14a,b$)), it results that a self-similar solution of the general case is possible only if within the same group (C5a–c) the term

$$\sqrt{1 + N \left| \frac{\partial H}{\partial X} \right|}, \tag{C6}$$

is invariant, equivalent to saying that H and X must have the same time dependence otherwise their ratio cannot match the units, already invariant under any transformation. This holds true only for $\gamma = 2$ since

$$N' \frac{\partial H'}{\partial X'} = N \frac{a^{F_1}}{a} \frac{\partial H}{\partial X} \to N' = N \quad \text{if } F_1 = 1. \tag{C7}$$

The general case can be approached by assuming that N is a further variable, instead of a parameter, and extending the group of transformations,

$$X' = aX, \quad T' = a^{F_2}T, \quad H' = a^{F_1}H, \quad N' = a^{1-F_1}N. \tag{C8a–d}$$

Assuming again T as fundamental variable, we have now three invariants within the transformation, namely $XT^{-r}, HT^{-s}, NT^{-m}$, where m is computed imposing the invariance of

$$\frac{N'}{T'^m} = \frac{a^{1-F_1}}{a^{mF_2}} \frac{N}{T}, \to m = \frac{1 - F_1}{F_2} \equiv \frac{\gamma - 2}{3}. \tag{C9}$$

The formal solution of the governing equations can be now expressed as

$$H = T^s g(XT^{-r}, NT^{-m}) \quad \text{or} \quad H = T^s g(\eta, \sigma), \quad \eta = XT^{-r}, \quad \sigma = NT^{-m}. \tag{C10}$$

We do not have further information on the structure of the function g. For progress, we can expand the function about $\sigma = 0$ for small values of σ,

$$g(\eta, \sigma) = g|_{(\eta,0)} + \left. \frac{\partial g}{\partial \sigma} \right|_{(\eta,0)} \sigma + O(\sigma^2). \tag{C11}$$

Following the same procedure in Di Federico *et al.* (2017) as detailed in Longo (2021b), we look for a perturbation of the fundamental first-order solution with an expansion in the regime $\sigma \equiv NT^{(\gamma-2)/3} \ll 1$,

$$H(X, T) = \xi_N^2 T^{(2\gamma-1)/3}[\Phi_0(\chi) + \sigma \Phi_1(\chi) + \cdots], \tag{C12}$$

$$X = \xi T^{(\gamma+1)/3}(1 + \sigma X_1 + \cdots), \tag{C13}$$

where $\Phi_0(\chi)$ and ξ_N are given by the first-order solution, and X_1 is a constant to be evaluated. The condition $\sigma \ll 1$ requires that (i) for $\gamma < 2$, $T \ll T_c \equiv N^{3/(2-\gamma)}$; and (ii) for $\gamma > 2$, $T \gg T_c$, T_c being the critical time. For $\gamma = 2$ the critical time becomes infinite and this corresponds to a self-similar solution for the full governing equations, without need of approximations, but requiring a different scaling of the variables as detailed in § 4.

Substituting (C12)–(C13) in (2.13)–($2.14a,b$), at $O(1)$ we recover the fundamental solution, with Φ_0 coincident with the solution of the governing equations (3.8) plus the constraints. The result at $O(\sigma)$ is

$$N \left(\Phi_1' \Phi_0 + \Phi_1 \Phi_0' \right)' + \chi \Phi_1' - (\gamma - 1)\Phi_1 = 0, \tag{C14}$$

which is a quasilinear ODE where Φ_0 is a forcing term, and that can be integrated with a further boundary condition at the nose of the current. The integral constraint ($2.14a,b$)

becomes

$$\xi_N (1 + \sigma X_1 + \ldots) \int_0^{1+\sigma X_1+\ldots} [\phi_0(\chi) + \sigma \Phi_1(\chi) + \ldots] \, \mathrm{d}\chi = 1, \qquad \text{(C15)}$$

which at $O(\sigma)$ yields

$$X_1 = -\frac{\int_0^1 \Phi_1(\chi) \, \mathrm{d}\chi}{\int_0^1 \Phi_0(\chi) \, \mathrm{d}\chi}. \qquad \text{(C16)}$$

REFERENCES

AURIAULT, J.-L., GEINDREAU, C. & ORGÉAS, L. 2007 Upscaling Forchheimer law. *Transp. Porous Med.* **70**, 213–229.

AUTELITANO, F., PETROLO, D., CHIAPPONI, L., GIULIANI, F. & LONGO, S. 2022 Temporary clogging effects induced by a sustainable anti-icing hydrogel on the hydraulic conductivity and inertia coefficient of open-graded asphalt pavements. *Constr. Build. Mater.* **361**, 129495.

BARENBLATT, G.I. 1952 On self-similar motions of compressible fluids in porous media. *Prikl. Mat. Mekh.* **16**, 679–698, in Russian.

BARREE, R.D. & CONWAY, M.W. 2004 Beyond beta factors: a complete model for Darcy, Forchheimer, and trans-Forchheimer flow in porous media. In *SPE Annual Technical Conference and Exhibition, Houston, Texas, September 2004*, paper no. SPE–89325. SPE.

CHOWDHURY, M.R. & TESTIK, F.Y. 2014 A review of gravity currents formed by submerged single-port discharges in inland and coastal waters. *Environ. Fluid Mech.* **14** (2, SI), 265–293.

CIRIELLO, V., DI FEDERICO, V., ARCHETTI, R. & LONGO, S. 2013 Effect of variable permeability on the propagation of thin gravity currents in porous media. *Intl J. Non-Linear Mech.* **57**, 168–175.

DE LOUBENS, R. & RAMAKRISHNAN, T.S. 2011 Analysis and computation of gravity-induced migration in porous media. *J. Fluid Mech.* **675**, 60–86.

DI FEDERICO, V., ARCHETTI, R. & LONGO, S. 2012 Similarity solutions for spreading of a two-dimensional non-Newtonian gravity current. *J. Non-Newtonian Fluid Mech.* **177–178**, 46–53.

DI FEDERICO, V., LONGO, S., KING, S.E., CHIAPPONI, L., PETROLO, D. & CIRIELLO, V. 2017 Gravity-driven flow of Herschel–Bulkley fluid in a fracture and in a 2D porous medium. *J. Fluid Mech.* **821**, 59–84.

EL-ZEHAIRI, A.A., MOUSAVI-NEHZAD, M., JOEKAR-NIASAR, V., GUYMER, I., KOURRA, N. & WILLIAMS, M.A. 2019 Pore-network modelling of non-Darcy flow through heterogeneous porous media. *Adv. Water Resour.* **131**, 103378.

FLETCHER, C.A.J. 1998 *One-Dimensional Diffusion Equation*, pp. 216–248. Springer.

FORCHHEIMER, P. 1901 Wasserbewegung durch boden. *Z. Verein. Deutsch. Ing.* **45**, 1788.

FOURAR, M., LENORMAND, R., KARIMI-FARD, M. & HORNE, R. 2005 Inertia effects in high-rate flow through heterogeneous porous media. *Transp. Porous Med.* **60**, 353–370.

FOURAR, M., RADILLA, G., LENORMAND, R. & MOYNE, C. 2004 On the non-linear behavior of a laminar single-phase flow through two and three-dimensional porous media. *Adv. Water Resour.* **27**, 669–677.

GARIBOTTI, C.R. & PÉSZYNSKA, M. 2009 Upscaling non-Darcy flow. *Transp. Porous Med.* **80**, 401–430.

GRIFFITHS, R.W. 2000 The dynamics of lava flows. *Annu. Rev. Fluid Mech.* **32**, 477–518.

HUPPERT, H.E. 1998 Quantitative modelling of granular suspension flows. *Phil. Trans. R. Soc.* A **356**(1747), 2471–2496, symposium on the Mechanics of Granular Materials in Engineering and Earth Sciences, London, England, Jan, 1998.

HUPPERT, H.E. 2006 Gravity currents: a personal perspective. *J. Fluid Mech.* **554**, 299–322.

HUPPERT, H.E. & NEUFELD, J.A. 2014 The fluid mechanics of carbon dioxide sequestration. *Annu. Rev. Fluid Mech.* **46**, 255–272.

HUPPERT, H.E. & WOODS, A.W. 1995 Gravity-driven flows in porous layers. *J. Fluid Mech.* **292**, 55–69.

LASSEUX, D. & VALDÉS-PARADA, F.J. 2017 On the developments of Darcy's law to include inertial and slip effects. *C. R. Méc.* **345**, 660–669.

LAURIOLA, I., FELISA, G., PETROLO, D., DI FEDERICO, V. & LONGO, S. 2018 Porous gravity currents: axisymmetric propagation in horizontally graded medium and a review of similarity solutions. *Adv. Water Resour.* **115**, 136–150.

LENCI, A., ZEIGHAMI, F. & DI FEDERICO, V. 2022 Effective Forchheimer coefficient for layered porous media. *Transp. Porous Med.* **144**, 459–480.

LI, L., LOCKINGTON, D.A., PARLANGE, M.B., STAGNITTI, F., JENG, D.-S., SELKER, J.S., TELYAKOVSKIY, A.S., BARRY, D.A. & PARLANGE, J.-Y. 2005 Similarity solution of axisymmetric flow in porous media. *Adv. Water Resour.* **28**, 1076–1082.

LONGO, S., CHIAPPONI, L., PETROLO, D., LENCI, A. & DI FEDERICO, V 2021 Converging gravity currents of power-law fluid. *J. Fluid Mech.* **918**, A5.

LONGO, S.G. 2021*a* Applications in fluid mechanics and hydraulics. In *Principles and Applications of Dimensional Analysis and Similarity*, pp. 177–218. Springer International Publishing.

LONGO, S.G. 2021*b* The structure of the functions of the dimensionless groups, symmetry and affine transformations. In *Principles and Applications of Dimensional Analysis and Similarity*, pp. 93–133. Springer International Publishing.

LUBE, G., BREARD, E.C.P., ESPOSTI-ONGARO, T., DUFEK, J. & BRAND, B. 2020 Multiphase flow behaviour and hazard prediction of pyroclastic density currents. *Nat. Rev. Earth Environ.* **1** (7), 348–365.

LYLE, S., HUPPERT, H.E., HALLWORTH, M., BICKLE, M. & CHADWICK, A. 2005 Axisymmetric gravity currents in a porous medium. *J. Fluid Mech.* **543**, 293–302.

MASSEY, B.S. 1971 *Units, Dimensional Analysis and Physical Similarity*. Van Nostrand Reinhold.

MATHIAS, S.A., DE MIGUEL GONZALEZ MARTINEZ, G.J., THATCHER, K.E. & ZIMMERMAN, R.W. 2011 Pressure buildup during CO_2 injection into a closed brine aquifer. *Transp. Porous Med.* **89** (3), 383–397.

MATHIAS, S.A., HARDISTY, P.E., TRUDELL, M.R. & ZIMMERMAN, R.W. 2009*a* Screening and selection of sites for CO_2 sequestration based on pressure buildup. *Intl J. Greenh. Gas Control* **3** (5), 577–585.

MATHIAS, S.A., HARDISTY, P.E., TRUDELL, M.R., ZIMMERMAN, R.W. & CARRERA, J. 2009*b* Approximate solutions for pressure buildup during CO_2 injection in brine aquifers. *Transp. Porous Med.* **79**, 265–284.

MATHIAS, S.A., MCELWAINE, J.N. & GLUYAS, J.G. 2014 Heat transport and pressure buildup during carbon dioxide injection into depleted gas reservoirs. *J. Fluid Mech.* **756**, 89–109.

MATSON, G.P. & HOGG, A.J. 2012 Viscous exchange flows. *Phys. Fluids* **24** (2), 023102.

MOODIE, T.B. 2002 Gravity currents. *J. Comput. Appl. Maths* **144** (1–2, SI), 49–83, International Symposium on Applied Mathematics, Dalian Univ. Technol., Aug. 2000.

MOUTSOPOULOS, K.N. 2009 Exact and approximate analytical solutions for unsteady fully developed turbulent flow in porous media and fractures for time dependent boundary conditions. *J. Hydrol.* **369** (1–2), 78–89.

MOUTSOPOULOS, K.N. & TSIHRINTZIS, V.A. 2005 Approximate analytical solutions of the Forchheimer equation. *J. Hydrol.* **309** (1), 93–103.

MULJADI, B.P., BLUNT, M.J., RAEINI, A.Q. & BIJELIC, B. 2017 The impact of porous media heterogeneity on non-Darcy flow behaviour from pore-scale simulation. *Adv. Water Resour.* **95**, 329–340.

NEUMAN, S.P. 1977 Theoretical derivation of Darcy's law. *Acta Mech.* **25**, 153–170.

PATTLE, R.E. 1959 Diffusion from an instantaneous point source with a concentration-dependent coefficient. *Q. J. Mech. Appl. Maths* **4**, 407–409.

PEGLER, S.S., HUPPERT, H.E. & NEUFELD, J.A. 2013 Topographic controls on gravity currents in porous media. *J. Fluid Mech.* **734**, 317–337.

PEGLER, S.S., HUPPERT, H.E. & NEUFELD, J.A. 2016 Stratified gravity currents in porous media. *J. Fluid Mech.* **791**, 329–357.

RIAZ, A. & CINAR, Y. 2014 Carbon dioxide sequestration in saline formations. Part I. Review of the modeling of solubility trapping. *J. Pet. Sci. Engng* **124**, 367–380.

RUTH, D. & MA, H. 1992 On the derivation of the Forchheimer equation by means of the averaging theorem. *Transp. Porous Med.* **7**, 255–264.

SCHNEIDER, L., DI CHIARA ROUPERT, R., SCHAEFER, G. & HELLUY, P. 2015 Highly gravity-driven flow of a NAPL in water-saturated porous media using the discontinuous Galerkin finite-element method with a generalised Godunov scheme. *Comput. Geosci.* **19** (4), 855–876.

SHEIKHI, S., SAHU, C.K. & FLYNN, M.R. 2023 Dispersion effects in porous medium gravity currents experiencing local drainage. *J. Fluid Mech.* **975**, A18.

SIDIROPOULOU, M.G., MOUTSOPOULOS, K.N. & TSIHRINTZIS, V.A. 2007 Determination of Forchheimer equation coefficients a and b. *Hydrol. Process.* **21** (4), 534–554.

SIMPSON, J.E. 1997 *Gravity Currents in the Environment and the Laboratory*. Cambridge University Press.

UNGARISH, M. 2018 Thin-layer models for gravity currents in channels of general cross-section area, a review. *Environ. Fluid Mech.* **18** (1, SI), 283–333, 4th International-Association-for-Hydro-Environment-Engineering-and-Research (IAHR) Congress, Liege, Belgium, Jul. 27–29, 2016.

VÁZQUEZ, J.L. 2007 *The Porous Medium Equation: Mathematical Theory*. Clarendon Press.

VILARRASA, V., BOLSTER, D., DENTZ, M., OLIVELLA, S. & CARRERA, J. 2010 Effects of CO_2 compressibility on CO_2 storage in deep saline aquifers. *Transp. Porous Med.* **85** (2), 619–639.

WHITAKER, S. 1996 The Forchheimer equation: a theoretical development. *Transp. Porous Med.* **25**, 27–61.

WOODS, A. 2015 *Flow in Porous Rocks: Energy and Environmental Applications*. Cambridge University Press.

WOODS, A.W. 1999 Liquid and vapor flow in superheated rock. *Annu. Rev. Fluid Mech.* **31**, 171–199.

ZEIGHAMI, F., LENCI, A. & DI FEDERICO, V. 2022 Drainage of power-law fluids from fractured or porous finite domains. *J. Non-Newtonian Fluid Mech.* **305**, 104832.

ZHANG, D., FAN, G., MA, L. & WANG, X. 2011 Aquifer protection during longwall mining of shallow coal seams: a case study in the Shendong Coalfield of China. *Intl J. Coal Geol.* **86** (2), 190–196.

ZHANG, T., ZHAO, Y., GAN, Q., YUAN, L., ZHU, G., CAI, Y. & CAO, B. 2018 Experimental investigation of Forchheimer coefficients for non-Darcy flow in conglomerate-confined aquifer. *Geofluids* **2018** (1), 4209197.

ZHENG, Z. & GRIGG, R. 2006 A criterion for non-Darcy flow in porous media. *Transp. Porous Med.* **63**, 57–69.

ZHENG, Z. & STONE, H.A. 2022 The influence of boundaries on gravity currents and thin films: drainage, confinement, convergence, and deformation effects. *Annu. Rev. Fluid Mech.* **54**, 27–56.